Central Asian moisture modulated by proto-Paratethys Sea incursions since the early Eocene

Niels Meijer, Guillaume Dupont-Nivet, Hemmo A. Abels, Mustafa Kaya, Alexis Licht, Meimei Xiao, Yang Zhang, Pierrick Roperch, Marc Poujol, Zhongping Lai, et al.

Article published in *Earth and Planetary Science Letters*

Niels Meijer, Guillaume Dupont-Nivet, Hemmo Abels, Mustafa Kaya, Alexis Licht, et al.. Central Asian moisture modulated by proto-Paratethys Sea incursions since the early Eocene. *Earth and Planetary Science Letters*, Elsevier, 2019, 510, pp.73-84. ⟨10.1016/j.epsl.2018.12.031⟩. ⟨insu-01990317⟩

Central Asian moisture modulated by proto-Paratethys Sea incursions since the early Eocene

Niels Meijer[a]; Guillaume Dupont-Nivet[abc]; Hemmo A. Abels[d]; Mustafa Y.Kaya[a]; Alexis Licht[e]; Meimei Xiao[f]; Yang Zhang[c]; Pierrick Roperch[b]; Marc Poujol[b]; Zhongping Lai[g]; Zhaojie Guo[c]

a Institute of Earth and Environmental Science [Potsdam]
b GR - Géosciences Rennes
c Key Laboratory of Orogenic Belts and Crustal Evolution - Ministry of Education
d TU Delft - Delft University of Technology
e University of Washington [Seattle]
f China University of Geosciences [Beijing]
g Institute of Marine Science

Abstract

The establishment and evolution of the Asian monsoons and arid interior have been linked to uplift of the Tibetan Plateau, retreat of the inland proto-Paratethys Sea and global cooling during the Cenozoic. However, the respective role of these driving mechanisms remains poorly constrained. This is partly due to a lack of continental records covering the key Eocene epoch marked by the onset of Tibetan Plateau uplift, proto-Paratethys Sea incursions and long-term global cooling. In this study, we reconstruct paleoenvironments in the Xining Basin, NE Tibet, to show a long-term drying of the Asian continental interior from the early Eocene to the Oligocene. Superimposed on this trend are three alternations between arid mudflat and wetter saline lake intervals, which are interpreted to reflect atmospheric moisture fluctuations in the basin. We date these fluctuations using magnetostratigraphy and the radiometric age of an intercalated tuff layer. The first saline lake interval is tentatively constrained to the late Paleocene–early Eocene. The other two are firmly dated between ~46 Ma (top magnetochron C21n) and ~41 Ma (base C18r) and between ~40 Ma (base C18n) and ~37 Ma (top C17n). Remarkably, these phases correlate in time with highstands of the proto-Paratethys Sea. This strongly suggests that these sea incursions enhanced westerly moisture supply as far inland as the Xining Basin. We conclude that the proto-

Paratethys Sea constituted a key driver of Asian climate and should be considered in model and proxy interpretations.

Keywords Paleogene**;** magnetostratigraphy**;** Central Asia**;** Xining Basin**;**westerlies**;**Asian monsoon

1. Introduction

Asia's modern-day climate is characterized by monsoons and inland deserts, but the timing and mechanism of their origin remains controversial. Both have been linked to the uplift of the Tibetan Plateau, the retreat of the proto-Paratethys Sea from Eurasia and the cooling of global climate (e.g. Ramstein et al., 1997, Dupont-Nivet et al., 2007, Zhang et al., 2007). Uplift of the Plateau would create orographic barriers and intensify monsoonal circulation by increasing thermal contrasts and insulating southern moist air (e.g. Molnar et al., 2010). Retreat of the proto-Paratethys Sea would remove a significant source of moisture from the Asian interior (Ramstein et al., 1997, Zhang et al., 2007; Bosboom et al., 2014a, Bosboom et al., 2014b; Bougeois et al., 2018) and may have strengthened the monsoons by increasing land-sea thermal contrasts (Ramstein et al., 1997, Zhang et al., 2007, Roe et al., 2016). The long-term global cooling during the Cenozoic (e.g. Cramer et al., 2009) could have induced the sea retreat by lowering the global sea level (Dupont-Nivet et al., 2007; Bosboom et al., 2014a, Bosboom et al., 2014b). Alternatively, the cooling may have caused aridification directly by weakening the hydrological cycle and the monsoons (Dupont-Nivet et al., 2007, Licht et al., 2014, Li et al., 2018a).

The Paleogene greenhouse period is key to understand the origin and mechanisms of Asian climate before significant Plateau uplift, sea retreat and global cooling had occurred. Early studies proposed that East Asia during this period was dominated by a subtropical arid belt with no monsoonal circulation (e.g. Guo et al., 2008). More recent studies show that the large-scale Asian atmospheric features were similar as today and that monsoons already existed during the Paleogene (Huber and Goldner, 2012; Licht et al., 2014, Licht et al., 2016; Quan et al., 2014, Caves et al., 2015, Roe et al., 2016). However, others suggest that these monsoons were only tropical and restricted to South Asia, while quasi-absent in East and Central Asia (Spicer et al., 2017, Li et al., 2018b).

Today, the low-level westerlies are the main source for atmospheric moisture in the region north of the Tibetan Plateau, which is shielded from the southerly

monsoons. Stable isotopes reveal that the westerlies have dominated this region since at least the late Paleocene (Caves et al., 2015, Bougeois et al., 2018), when a proto-Tibetan Plateau already created an orographic barrier from the south (e.g. Molnar et al., 2010). During the Paleogene, the westerlies may have carried additional moisture from the proto-Paratethys Sea (Zhang et al., 2007, Roe et al., 2016, Bougeois et al., 2018), which extended from the Mediterranean up to western China at this time (e.g. Bosboom et al., 2014a, Bosboom et al., 2014b). The extent of this sea fluctuated with three progressively smaller sea incursions that are superimposed on a long-term retreat. These are now well-constrained in time and space by new paleogeographic analyses (Bosboom et al., 2014a, Bosboom et al., 2014b; Kaya et al., 2018). During highstands, the sea extended far into the Tarim Basin of western China, whereas during lowstands it retreated entirely beyond Tajikistan (Bosboom et al., 2014a, Bosboom et al., 2014b; Kaya et al., 2018). These incursions may have modulated the moisture carried by the westerlies and affected precipitation in western China (Bosboom et al., 2014a, Bosboom et al., 2014b; Bougeois et al., 2018).

The Xining Basin, located on the northeastern margin of the Tibetan Plateau (Fig. 1), provides an exceptional sedimentary record to understand Asian atmospheric circulation during the Paleogene. It contains quasi-continuous terrestrial mudrocks throughout the Cenozoic, which can be dated using magnetostratigraphy (e.g. Dai et al., 2006). Sedimentological and palynological studies show that these deposits reflect atmospheric moisture variations which are interpreted as the interplay between East Asian monsoons and westerlies (Abels et al., 2011, Bosboom et al., 2014c; Dupont-Nivet et al., 2007, Dupont-Nivet et al., 2008a). However, the Xining record has not been accurately dated and described before the late Eocene (~40–34 Ma). Therefore, the climatic effects of the India–Asia collision, the earlier proto-Paratethys Sea incursions and the onset of global cooling, all occurring during the early to middle Eocene (~56-40 Ma), remain unknown.

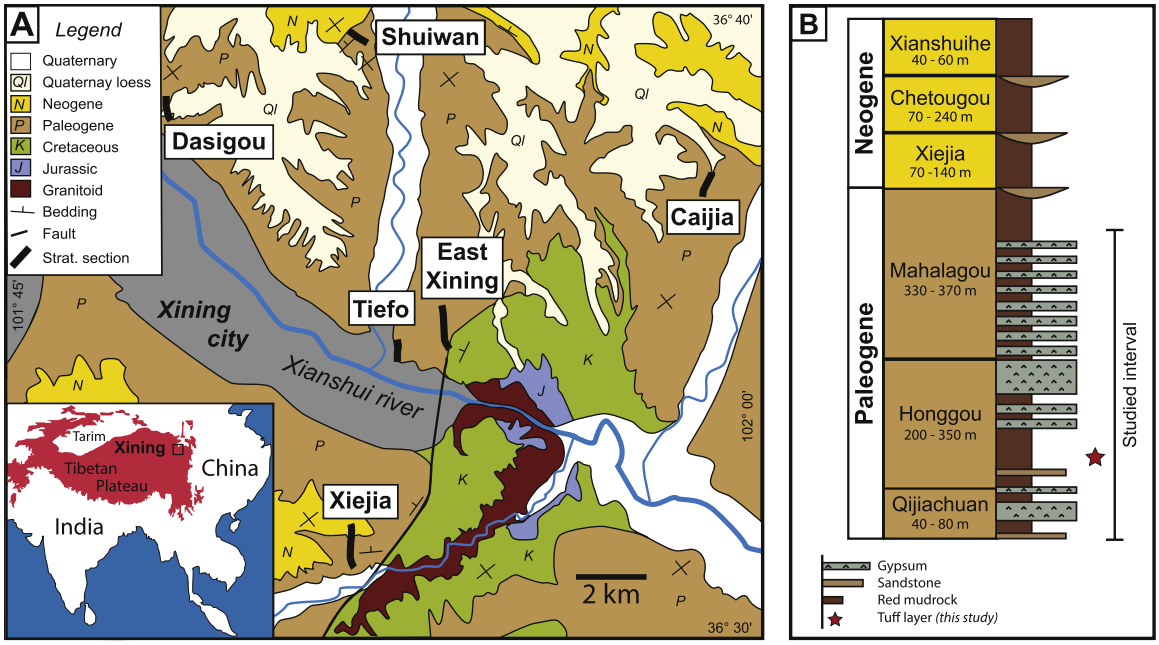

Fig. 1. (A) Regional geological map (QBGMR, 1985) showing the locations of the sections examined here and in previous studies. Inset map shows the location of the Xining Basin along the margin of the northeastern Tibetan Plateau. (B) Generalized stratigraphic column modified from Horton et al. (2004), listing formations, thicknesses and lithologies.

In this study, we extend the litho- and magnetostratigraphy of the upper Eocene – Miocene deposits in the Xining Basin (Abels et al., 2011, Xiao et al., 2012, Bosboom et al., 2014c) to the lower Eocene where the magnetostratigraphy remained unreliable so far (Horton et al., 2004, Dai et al., 2006). We analyzed three laterally equivalent sections for magnetostratigraphy and complemented our correlations of the polarity zones with the radiometric age of a tuff layer. Furthermore, we interpret the evolution of atmospheric moisture and its driving mechanisms throughout the early Eocene to Oligocene epochs using our detailed lithostratigraphic descriptions and previous records from the Xining Basin.

2. Geologic setting

The Xining Basin forms the western part of the Cenozoic Longzhong Basin, which subsequently segmented into smaller sub-basins during deformation in the Miocene (Horton et al., 2004). The origin of the basin during the Paleogene is unclear and is hypothesized to be an extensional basin either due to thermal subsidence (Horton et al., 2004) or differential clockwise-rotation of crustal blocks (Zhang et al., 2016). Alternatively, the basin may have formed as a foreland basin of the Western Qinling Shan, a mountain range located ~80 km to the south (Clark et al., 2010).

The Paleogene strata of the Xining Basin are composed of red gypsiferous mudrocks and gypsum beds and include the Qiejiachuan, Honggou and Mahalagou Formations (Fig. 1B; QBGMR, 1985). The depositional environment is interpreted as a distal arid mudflat based on the lack of fluvial channels, the widespread occurrence of evaporites and the massive structure of the mudrocks resulting from subaerial reworking (Smoot and Lowenstein, 1991, Talbot et al., 1994, Dupont-Nivet et al., 2007, Abels et al., 2011). Provenance analysis shows that the fluvio-lacustrine deposits were mostly derived from distal highlands such as the Western Qinling Shan in the south and the Qilian Shan in the north (Zhang et al., 2016). The rest of the sediments were transported as eolian dust from reworked fluvial deposits and, to a minor extent, from the Qaidam Basin in the west (Licht et al., 2014, Licht et al., 2016).

Gypsum is formed by evaporating surface- or groundwater and accumulates to form gypsum beds when groundwater tables are sufficiently close to the surface to replenish the brine with the necessary solutes (Rosen, 1994, Dupont-Nivet et al., 2007, Abels et al., 2011). In well-drained settings with a deeper groundwater table, the evaporites are unlikely to be preserved (Rosen, 1994) and subaerially oxidized mudrocks accumulate instead (Dupont-Nivet et al., 2007, Abels et al., 2011). Basin-wide alternations between red mudrocks and saline lake evaporites therefore indicate changes in the groundwater table and are interpreted to reflect variations in atmospheric moisture in the catchment (Dupont-Nivet et al., 2007, Abels et al., 2011).

3. Methods

3.1. Sections

We resampled and analyzed at higher resolution the previously published East Xining (36°34′ 50″ N, 101°53′ 42″ E) and Xiejia (36°31′ 20″ N, 101°52′ 20″ E) sections (Horton et al., 2004, Dai et al., 2006) and added the newly sampled Caijia section (36°36′ 55″ N, 101°59′ 3″ E). Stratigraphic thicknesses were measured using a Jacob's staff and detailed lithological logs were made in the field.

3.2. U–Pb dating of a tuff

A tuff layer from the Xiejia section was processed for U–Pb radiometric dating. After crushing and grinding, the powder was separated using magnetic and heavy liquid separation. The zircon crystals were handpicked under a binocular microscope, mounted on a 25 mm ring of epoxy, grinded, polished and imaged

using cathodoluminescence. In total, 31 zircon crystals were collected from the tuff sample and U–Pb dating was conducted by in-situ laser ablation inductively coupled plasma mass spectrometry (LA-ICPMS) at Géosciences Rennes, France. Detailed analytical procedures and individual data are reported in the supplementary material. Additionally, three tuff samples were crushed and melted to make tablets for X-Ray Fluorescence (XRF) analysis to identify the chemical composition. The XRF analysis was performed using a PANalytical AXIOS Advanced at the German Research Center for Geosciences (GFZ), Potsdam, Germany.

3.3. Magnetostratigraphy

Paleomagnetic samples were collected at the sections with a resolution of ~0.5 to 1 meter where possible. Sampling was conducted using a portable electric drill and a compass mounted on an orientation stage. The paleomagnetic samples were thermally demagnetized with 10–15 temperature steps up to 680 °C. Samples from the Caijia section, and the lower 105 m of the Xiejia section were analyzed at Géosciences Rennes, France. Samples from the East Xining section and the upper 91 m of the Xiejia section were analyzed at the Paleomagnetic Laboratory 'Fort Hoofddijk' of the Faculty of Geosciences at Utrecht University, the Netherlands.

4. Lithostratigraphy

The measured sections (Fig. 2) are subdivided in formations following the classification of the Qinghai Bureau of Geology and Mineral Resources (QBGMR, 1985). In the following, these formations are described and interpreted in terms of depositional environment. Detailed logs are provided in the supplementary material (Fig. S1).

4.1. Lower Qiejiachuan Formation

4.1.1. Description

The lower part of the Qiejiachuan Formation (~20 m thick) consists of massive red mudrocks (2.5YR 4/4) interbedded with a few massive sandstone beds. Occasionally, the mudrocks contain slickensides and centimeter-scale horizons of grey (5GY 5/1) mottling. The sandstone beds are up to a few decimeters thick, fine- to coarse-grained and laterally extensive.

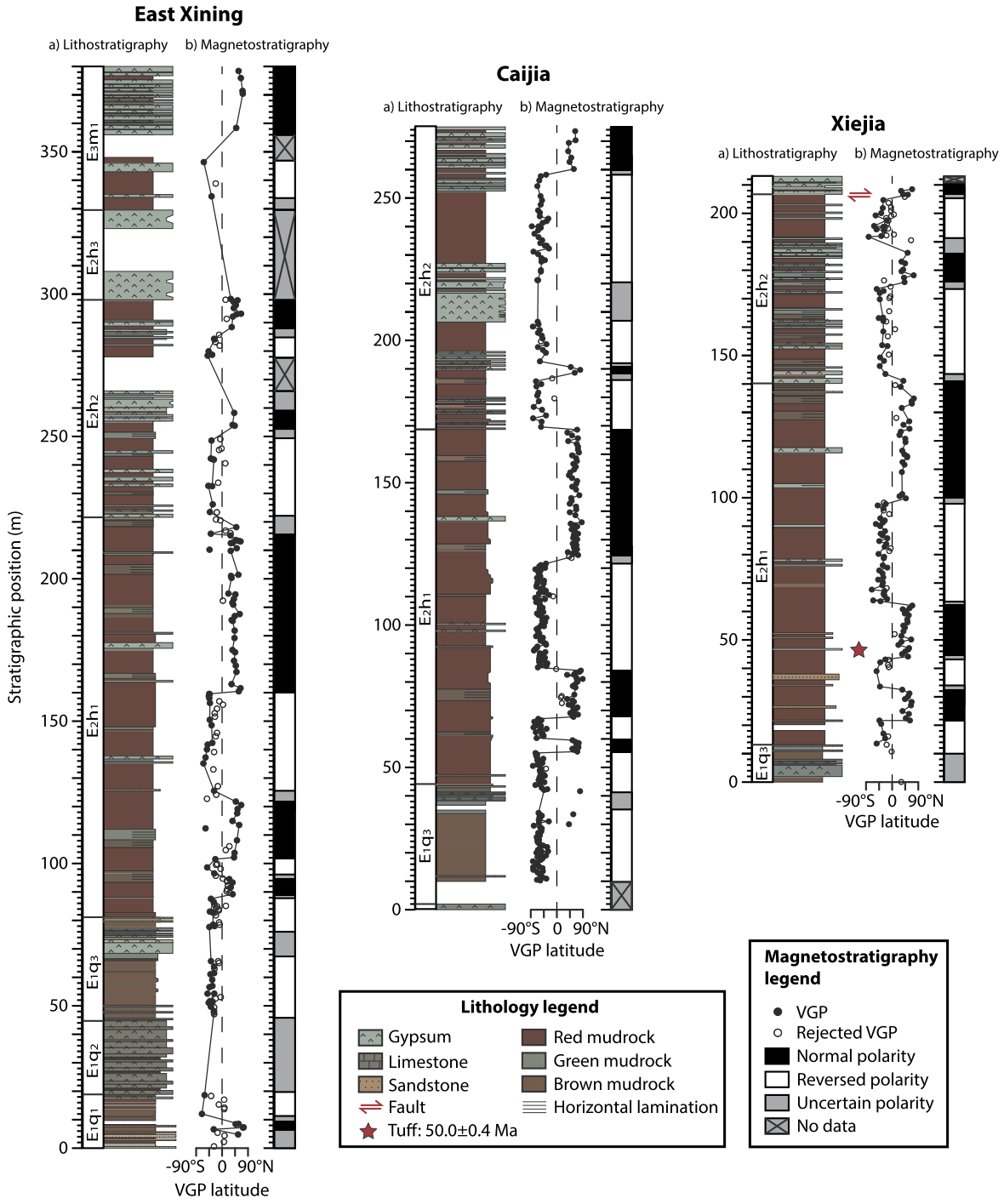

Fig. 2. The East Xining, Caijia and Xiejia sections showing (a) the lithostratigraphy and (b) the magnetostratigraphy with Virtual Geomagnetic Pole (VGP) latitudes and corresponding polarity zones.

4.1.2. Interpretation

The dominance of massive, oxidized mudrocks indicates deposition on a subaerially exposed mudflat (Smoot and Lowenstein, 1991, Dupont-Nivet et al., 2007, Abels et al.,

2011). The lateral extent and massive structure of the sandstone beds suggests deposition by unconfined fluvial flows (North and Davidson, 2012).

4.2. Middle Qiejiachuan Formation

4.2.1. Description

The middle Qiejiachuan Formation (~30 m thick) is characterized by a laterally extensive package of gypsum beds. The beds are decimeters thick and alternate between light gray (10Y 5/1), indurated intervals and dark grey (N 3/1), less indurated, organic-rich (TOC = ~0.7–1.7%) intervals (Fig. 3A). The gypsiferous beds are nodular, but reveal centimeter-scale horizontal lamination in fresh, unweathered outcrops (Fig. 3A).

4.2.2. Interpretation

The gypsum and horizontal lamination indicate deposition in a saline lake (Smoot and Lowenstein, 1991, Dupont-Nivet et al., 2007, Abels et al., 2011). The alternations between gypsiferous and carbonaceous beds may reflect fluctuating salinity and/or productivity (Potter et al., 2005).

4.3. Upper Qiejiachuan Formation

4.3.1. Description

The upper Qiejiachuan Formation (~30 m thick) consists of massive mudrocks with a characteristic liver-brown color (5YR 4/2, Fig. 3B). The mudrocks contain specks of organic debris, abundant slickensides and are commonly interbedded with centimeter-scale beds of coarse silt with ripple laminations. Centimeter-scale carbonate beds composed of micrite occur in the lower part. The top of the Qiejiachuan Formation consists of a ~5 meters-thick interval containing green (5GY 5/1) gypsiferous mudrocks and decimeter-scale beds of massive gypsum. The mudrocks are interbedded with centimeter-scale beds of micritic carbonate.

4.3.2. Interpretation

The lack of horizontal lamination and abundance of slickensides in the mudrocks indicate deposition on a subaerially exposed mudflat (Smoot and Lowenstein, 1991, Dupont-Nivet et al., 2007, Abels et al., 2011). The organic debris admixed with red regolith results in the characteristic liver-brown color (Potter et al., 2005). The rippled beds of coarse siltstones are interpreted to be deposited in episodic events of surface flow (North and Davidson, 2012). The carbonates may represent deposition in local, relatively freshwater ponds (Smoot and Lowenstein, 1991). The gypsum beds at

the top indicate deposition in a saline lake (Smoot and Lowenstein, 1991, Abels et al., 2011).

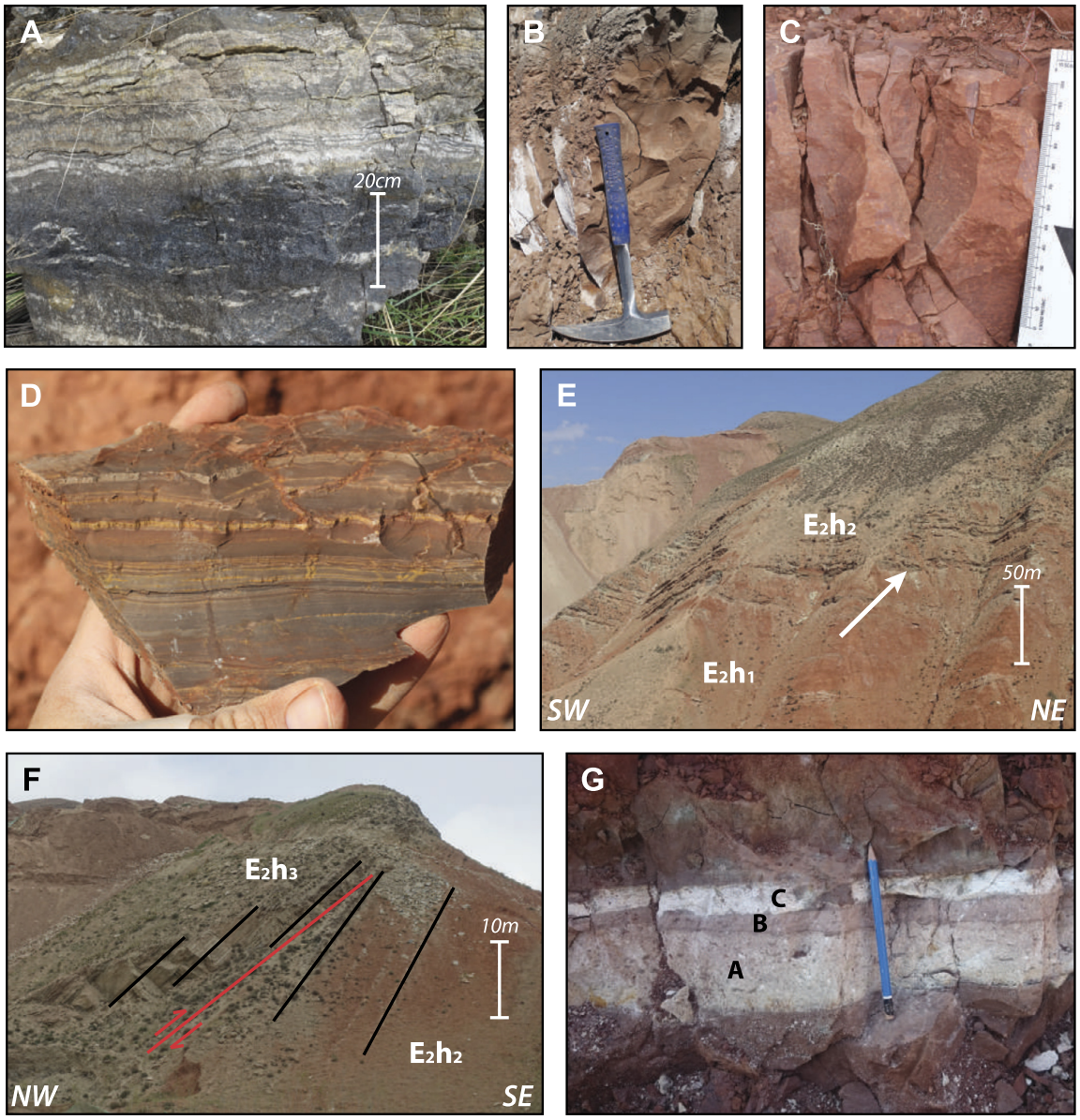

Fig. 3. Field photos showing: (A) an alternation between carbonaceous and gypsiferous beds in the middle Qiejiachuan Formation. Note the horizontal laminations in the upper part. (B) Massive liver-brown mudrock in the upper Qiejiachuan Formation. Hammer for scale. (C) Massive brick-red mudrock in the lower Honggou Formation showing mm-scale burrows. Scale-bar on the right. (D) Finely laminated brown mudrock in the lower Honggou Formation showing mudcracks and micrite laminae. (E) Overview of the Xiejia section showing the Honggou Formation. Arrow indicates the transition from the lower to middle Honggou Formation at the 140 meter-level. Scale-bar on the right (F) Overview of the top of the Xiejia section showing a fault at the base of the upper Honggou Formation. Scale-bar on the right. (G) A tuff bed in the Xiejia section at the 46.3 meter-level showing the three different layers that were geochemically analyzed (A, B and C). Pencil for scale.

4.4. Lower Honggou Formation

4.4.1. Description

The lower Honggou Formation (~130 m thick) is characterized by brick-red (2.5 YR 4/6) massive mudrocks (Fig. 3C). The mudrocks are commonly interbedded with centimeter-scale beds of rippled coarse siltstones. Rare cross-bedded sandstones occur as decimeter-scale beds in the lower part of the more proximal Xiejia section. The red mudrocks of the Honggou Formation contain abundant millimeter-scale interstitial gypsum nodules. Millimeter-scale burrows, slickensides, blocky peds and grey (10GY 7/1) mottling are common, but millimeter-scale carbonate nodules are rare. The red mudrocks occasionally contain <5 meters-thick intervals of brown (5YR 4/2) mudrocks with millimeter-scale lamination (Fig. 3D). These intervals contain specks of organic debris, slickensides, desiccation cracks and centimeter-scale beds of micritic carbonate and gypsum. The red mudrocks are rarely interbedded with green (10GY 6/1), decimeter-scale beds of gypsum with either a nodular structure or centimeter-scale horizontal lamination.

4.4.2. Interpretation

The dominance of gypsiferous red mudrocks indicates deposition on a subaerially exposed arid mudflat (Smoot and Lowenstein, 1991, Dupont-Nivet et al., 2007, Abels et al., 2011), with occasional fluvial events evidenced by the coarse silt- and sandstone beds (North and Davidson, 2012). The laminated brown mudrock intervals are interpreted as lacustrine deposits. However, the observed desiccation cracks and slickensides suggest that these lakes were shallow and occasionally exposed to drying. The gypsum beds are interpreted as saline lake deposits (Smoot and Lowenstein, 1991, Abels et al., 2011).

4.5. Middle Honggou Formation

4.5.1. Description

A sudden increase in gypsum beds and mudrocks with fine horizontal laminations marks the transition (Fig. 3E) to the middle Honggou Formation (~80 m thick). The laminated mudrocks range in color from brown (5YR 4/3) to green (10GY 6/1). Massive red mudrocks occur as well, but are less abundant than in the lower Honggou Formation. The gypsum beds are green (10GY 6/1), laminated or nodular, and range in thickness from decimeter- to meter-scale. The middle Honggou Formation can be traced

regionally as a more gypsiferous interval. However, individual beds are laterally discontinuous between sections spaced up to 14.5 km.

4.5.2. Interpretation

The massive red mudrocks, laminated mudrocks and gypsum beds are interpreted to be deposits of subaerially exposed mudflat, lake and saline lake environments respectively (Smoot and Lowenstein, 1991, Dupont-Nivet et al., 2007, Abels et al., 2011). The lateral discontinuity of the beds suggests that the lacustrine mudrocks and evaporites accumulated in local topographic depressions whereas oxidized mudflats formed on local highs. The nodular character of the gypsum beds is likely due to weathering because it is absent in fresh outcrops (Abels et al., 2011).

4.6. Upper Honggou Formation

4.6.1. Description

The upper Honggou Formation consists of a ~10–30 meters-thick gypsum package containing decimeter-scale beds of massive to nodular gypsum as well as macro-crystalline gypsum and glauberite (Bosboom et al., 2014c). A minor fault observed at the base of the gypsum package in the Xiejia section may have resulted in a hiatus (Fig. 3F). Locally, the gypsum package can be replaced by fluvial sandstone beds, as observed in the Dasigou section, north of Xining (Fig. 1A; Bosboom et al., 2014c).

4.6.2. Interpretation

The thick accumulation of gypsum beds indicates prolonged deposition in a saline lake (Smoot and Lowenstein, 1991, Abels et al., 2011, Bosboom et al., 2014c). The beds containing euhedral macro-crystals suggest that the lake was perennial at times (Smoot and Lowenstein, 1991, Bosboom et al., 2014c). Although the thickness of the gypsum package varies, the upper Honggou Formation is characteristic and can be correlated across the basin (Horton et al., 2004).

4.7. Lower Mahalagou Formation

4.7.1. Description

The lower Mahalagou Formation (~70 m thick) is characterized by meter-scale alternations between red mudrocks and gypsum beds that can be correlated between the studied sections (Dupont-Nivet et al., 2007, Abels et al., 2011, Bosboom et al., 2014c). The mudrocks have a massive structure, whereas the gypsum beds vary between a massive, laminated or nodular structure (Abels et al., 2011). An interval of reddish brown (5YR 4/3) mudrocks with a thickness of ~20 m occurs at the base.

4.7.2. Interpretation

The Mahalagou Formation has been described extensively in previous studies and is interpreted as deposits of astronomically forced cycles between subaerial mudflats and saline lakes (Dupont-Nivet et al., 2007, Abels et al., 2011, Bosboom et al., 2014c).

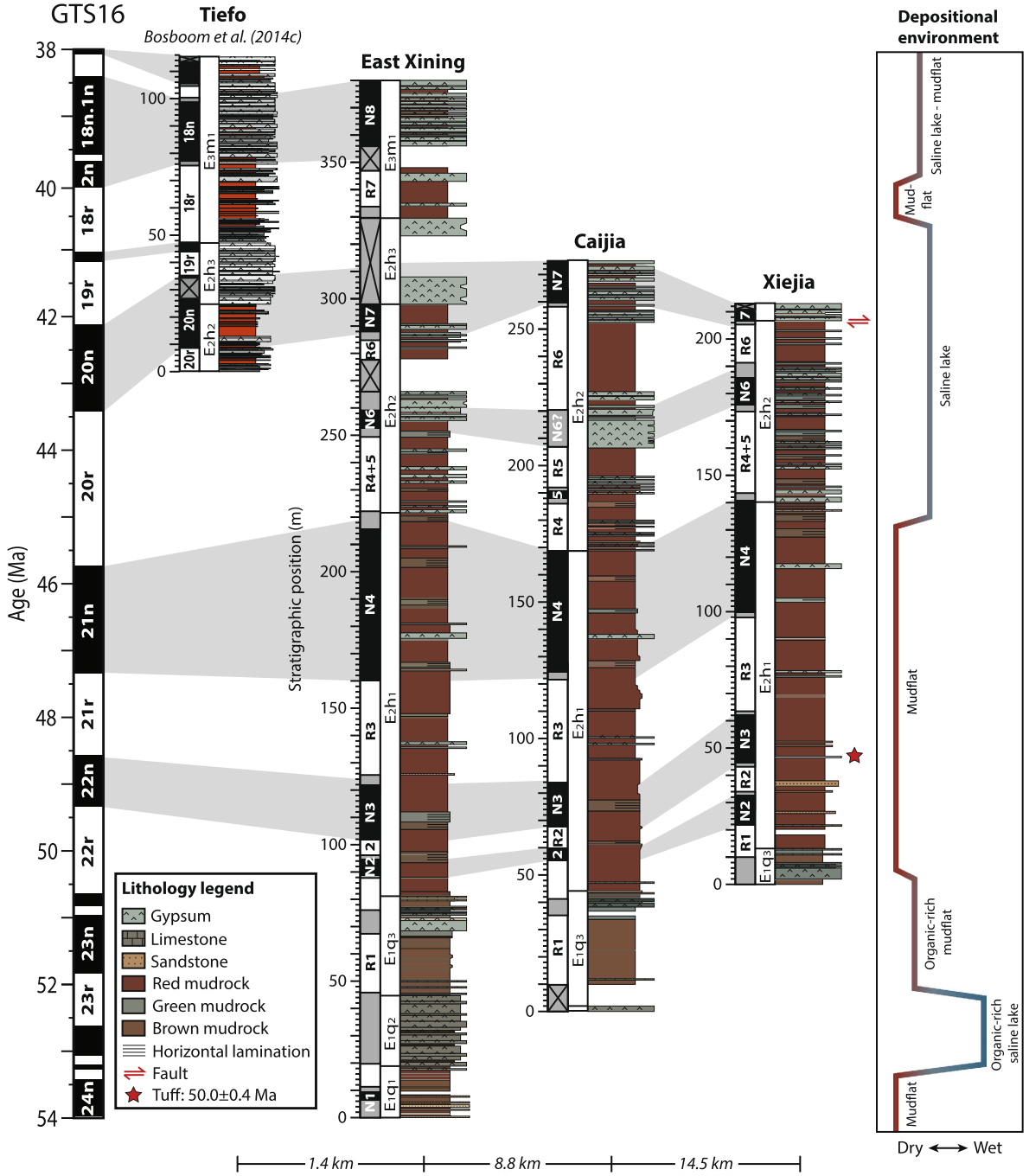

Fig. 4. Magnetostratigraphic correlations between the three studied sections and the Tiefo section (Bosboom et al., 2014c). The chrons are correlated to the GTS16 (Ogg et al., 2016). Trends in the dominant depositional environment are shown on the right.

5. U–Pb radiometric dating of a volcanic tuff

4.8. Summary

Throughout the studied interval, we observe several trends in the depositional environments (Fig. 4). A decrease in organic matter indicates a long-term aridification in the record. Organic-rich deposits are abundant in the Qiejiachuan Formation, occur sporadically throughout the overlying Honggou Formation and disappear in the lower Mahalagou Formation along with carbonate beds (Bosboom et al., 2014c). Superimposed on this long-term drying we observe shorter term alternations between mudflat deposits and evaporites (Fig. 4). The middle Qiejiachuan Formation is dominated by saline lake deposits and is overlain by organic-rich mudflat deposits of the upper Qiejiachuan Formation and red mudrocks of the lower Honggou Formation. These mudflat deposits are followed by a shift to lacustrine mudrocks and evaporites in the overlying middle to upper Honggou Formation. This is followed by a ~20 meters-thick interval of mudflat deposits at the base of the overlying Mahalagou Formation, after which this formation is dominated by characteristic mudrock–evaporite cycles.

5.0 U–Pb radiometric dating of a volcanic tuff

A volcanic tuff with a thickness of 12 cm was identified in the Xiejia section at the 46.3 meter-level (Fig. 3G) and is used to constrain the age of the deposits. The tuff is composed of three different layers and consists predominantly of vitreous matrix. The layers have similar chemical compositions (Table S1) and are classified, on an anhydrous basis, as trachyte (Fig. S2) according to the classification of Le Maitre et al. (1989). However, the relatively high concentration of volatiles (LOI = ~8%) indicates that this tuff may have been altered.

Of the 31 zircon crystals that were analyzed, 19 analyses plot in a concordant to sub-concordant position (99 to 80%, Fig. 5A), indicating the presence of a slight amount of common Pb in some of the zircon grains and/or a very small Pb loss. Their weighted average 206Pb/238U age (Fig. 5B) is well defined at 50.2 ± 0.4 Ma (MSWD = 1.9). This mean age is equivalent within error with the lower intercept date of 50.0 ± 0.4 Ma (Fig. 5A) if the discordia is forced to a 207Pb/206Pb value of 0.839 ± 0.01 calculated (at 50 ± 10 Ma) following the Pb evolution model of Stacey and Kramers (1975). This is also similar to the Tuffzirc age (Ludwig and Mundil, 2002) of 50.15 +0.65/−0.45 Ma. We therefore conclude that this tuff was deposited at 50.0 ± 0.4 Ma.

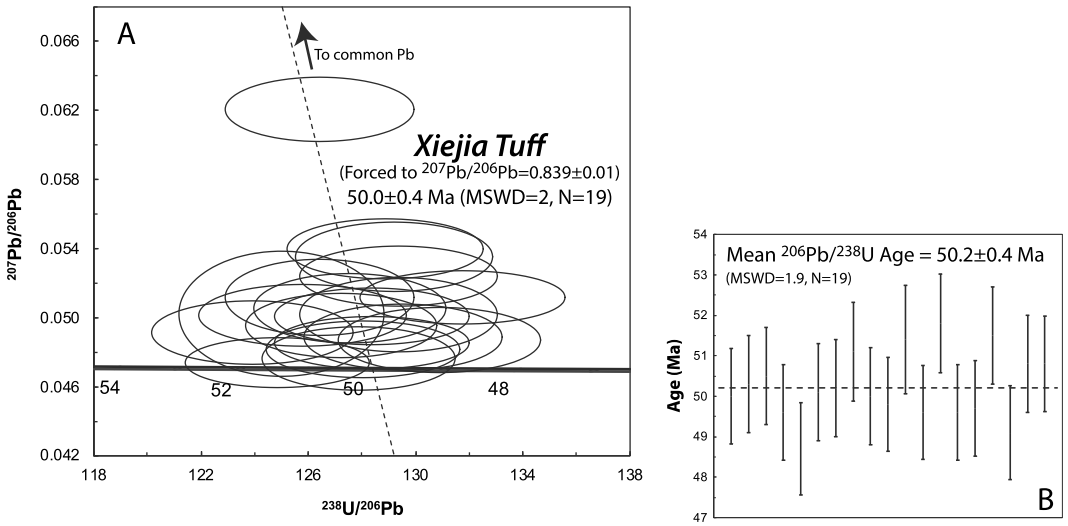

Fig. 5. (A) Tera–Wasserburg diagram for the youngest group of zircons. (B) Weighted average 206Pb/238U Age for the same 19 zircon grains. All ellipses and apparent 206Pb/238U ages are plotted at 2σ.

The remaining 12 crystals produced apparent ages ranging from 237 to 2450 Ma and are interpreted as xenocrystic in origin. The Eocene volcanic belt throughout the northern Qiangtang terrane provides a possible source for the tuff, since multiple ages reported here fit well within the error range of our tuff sample (Chapman and Kapp, 2017).

6. Magnetostratigraphy

Paleomagnetic analysis is used to identify reversals and further constrain the age of the deposits.

6.1. Thermal demagnetization

Demagnetization of the red mudrock samples up to 200–300 °C resulted in the removal of a secondary normal overprint and is followed by a linear decay towards the origin (Fig. S3). A drop in magnetization is observed between 550–680 °C indicating a combination of hematite and magnetite as the dominant ferromagnetic carriers (Fig. S3). Samples from the gypsum beds have a lower magnetization and showed erratic directions that could not be interpreted. The magnetic behavior is similar as observed in previous studies in the Xining Basin (Dai et al., 2006, Dupont-Nivet et al., 2007, Dupont-Nivet et al., 2008b; Abels et al., 2011, Xiao et al., 2012, Bosboom et al., 2014c).

6.2. ChRM directions

Characteristic remanent magnetization (ChRM) directions of the samples were calculated by eigenvector principal component analysis (Kirschvink, 1980) on at least

four temperature steps showing a linear decay between 300–600 °C. Maximum angular deviations (MAD) were estimated for all calculated ChRM directions. All samples have a MAD <30° and most are <10°.

Virtual geomagnetic poles (VGPs) were calculated from the ChRM directions and the VGP latitudes are shown in Fig. 2 and Fig. S1. The VGPs show two clusters of either normal (positive latitude) or reversed (negative latitude) polarity. Samples with a VGP of more than 45° from the mean normal or reversed VGP are considered outliers and removed from further analysis (open symbols in Fig. 2 and Fig. S1, red symbols in Fig. S4).

The means for both the normal and reversed ChRM directions were calculated for each section (Fig. S4) using Fisher statistics (Fisher, 1953). Reversals tests (McFadden and McElhinny, 1990) performed on the mean directions of the sections are negative indicating that the angle between the mean normal and reversed polarities is larger than the critical angle. These negative reversals tests are due to an unresolved normal overprint as observed in previous studies in the Xining Basin (Dupont-Nivet et al., 2008b, Xiao et al., 2012, Bosboom et al., 2014c). This is especially evident in the Xiejia and East Xining sections (Fig. S4), which are more tilted (dip of ~50°) compared to the Caijia section (dip of ~7°). The normal overprint would preclude the use of these datasets for tectonic rotation analysis but it does not affect the reliability of the magnetostratigraphy used in this study as discussed further below.

6.3. Correlation to the GTS

Polarity zones are identified by at least two successive samples of the same polarity and are labeled N1 to N8 and R1 to R7 (Fig. 4). The magnetostratigraphy is laterally similar and can be readily correlated between the studied sections. However, normal zone N5 is only observed in the Caijia section. This zone with a thickness of only 2–4 m is probably missed in the other sections due to a lower resolution of reliable VGP's. Zone N6 is lacking in the Caijia section because no magnetic signal is recorded in the gypsum beds of this interval.

In the following, the polarity zones are correlated to chrons (Fig. 4) in the geological timescale (GTS16, Ogg et al., 2016). The tuff, located at the base of normal polarity zone N3, provides a tie point for our correlation. The only normal chron with a basal age near 50 ± 0.4 Ma is C22n, which has a basal age of 49.3 Ma in the GTS16, but was recently tuned to 49.7 Ma (Westerhold et al., 2017). The latter age fits well within the error range

of the tuff. Zone N3 is therefore correlated to C22n. The overlying zones R3 and N4 are then correlated to C21r and C21n respectively. C21n is followed by a relatively long reversed and a long normal chron (C20r and C20n) in the timescale that were both identified at the base of the Tiefo section (Bosboom et al., 2014c). It follows that polarity zone N7 can be correlated to C20n by using the characteristic gypsum package of the upper Honggou Formation as a marker bed. Zones R7 and N8 in the East Xining section are subsequently correlated to C18r and C18n by using the gypsum cycles of the Mahalagou Formation as marker beds. Following the above, zones R4 to R6 are unequivocally correlated to C20r. The resulting age model shows stable accumulation rates of ~3 cm/kyr in the Honggou Formation (Fig. S5), which is similar to rates observed in the overlying sections (Abels et al., 2011, Xiao et al., 2012; Bosboom et al., 2014c). This suggests an absence of major hiatuses and further supports our correlation. However, the short normal zones N5 and N6 (with thicknesses of 5 to 10 m) remain uncorrelated in our interpretation. No such zones are observed in C20r of the geological timescale. Zone N2, located just below N3, is uncorrelated as well because a correlation to C23n would result in an unusually low accumulation rate of ~0.6 cm/kyr in both R2 (when correlated to C22r) and N2 (when correlated to C23n). To our knowledge, short normal chrons that could relate to N2, N5 and N6 have not been reported in any published marine or terrestrial records of this interval (e.g. Fig. 6 in Turtù et al., 2017 and references therein). Bouligand et al. (2006) record nine cryptochrons in C20r and three in C22r based on stacked marine magnetic anomaly profiles. Most of these cryptochrons have a short duration of less than 8 kyrs, but three have relatively long durations of 12 to 14 kyrs (C20r-5, C20r-6 and C22r-1). These three longer cryptochrons could fit with the stratigraphic positions of the short normal zones in the Xining Basin. However, this would imply anomalously high accumulation rates of at least ~35 cm/kyr for these cryptochrons to be recorded in the observed >5 meters-thick normal zones. Therefore, a more probable hypothesis is that these zones result from secondary magnetizations occurring in stratigraphic intervals prone to remagnetization. However, we found no clear differences in lithologies (Fig. 2, S1), magnetic behavior (Fig. S3) and ChRM directions (Fig. S4) compared to the other polarity zones. Nevertheless, the pervasive secondary normal overprint evidenced by the failed reversals tests suggests that some stratigraphic intervals may have been overprinted.

The age of the Qiejiachuan Formation cannot be constrained due to the low resolution of reliable VGP latitudes in the gypsum interval of the middle Qiejiachuan Formation. This hinders the record of the expected polarity zones below the radiometric age of the tuff (50.0±0.4 Ma) and thus prevents a reliable downward extension of the magnetostratigraphic correlation.

7. Discussion

Our magnetostratigraphic correlations indicate that the Honggou Formation spans from ~50 Ma (C22r) to ~41 Ma (top of C19n). This extends the dated stratigraphic record to cover the early Eocene to Oligocene epochs (Fig. 6; Abels et al., 2011, Xiao et al., 2012, Bosboom et al., 2014c). Our age model agrees broadly with the preferred correlations reported in Dai et al. (2006), except for two notable differences: (1) our record shows that N22 in Dai et al. (2006) consists of two separate normal zones. The upper of these is correlated to C22n, which is now further constrained by the age of the tuff. The lower is interpreted here as a remagnetized normal zone. (2) N23 in Dai et al. (2006) is not observed in this study and is likely a result of remagnetized samples from this gypsiferous interval. Therefore, the previously proposed correlation of the base of the Xiejia section to ~52 Ma (Dai et al., 2006) is revised by our results to ~50 Ma. Our paleo-environmental record shows a long-term drying trend from ~50 to 40 Ma (Fig. 4, Fig. 6), which is corroborated by previous rock magnetic analyses in the basin (Fang et al., 2015). This drying trend persists in the overlying deposits, where the disappearance of organic-rich deposits and carbonate beds in the Mahalagou Formation is synchronous with an aridification step in the pollen record between 40.6 and 39.4 Ma (Bosboom et al., 2014c). Successive aridification steps are then recorded by a decrease in gypsum beds at ~37 Ma ('Step 1', Abels et al., 2011), an increase in accumulation rate at ~35 Ma ('Step' 2, Abels et al., 2011) and the final disappearance of saline lakes at the Eocene–Oligocene Transition (EOT; Dupont-Nivet et al., 2007). This long-term aridification of the Xining Basin has been linked to Tibetan Plateau uplift (Li et al., 2018a), long-term proto-Paratethys Sea retreat (Dupont-Nivet et al., 2007, Abels et al., 2011; Bosboom et al., 2014a, Bosboom et al., 2014b) and global cooling (Dupont-Nivet et al., 2007, Abels et al., 2011, Bosboom et al., 2014c, Fang et al., 2015, Li et al., 2018a) and is likely the result of a combination of these mechanisms.

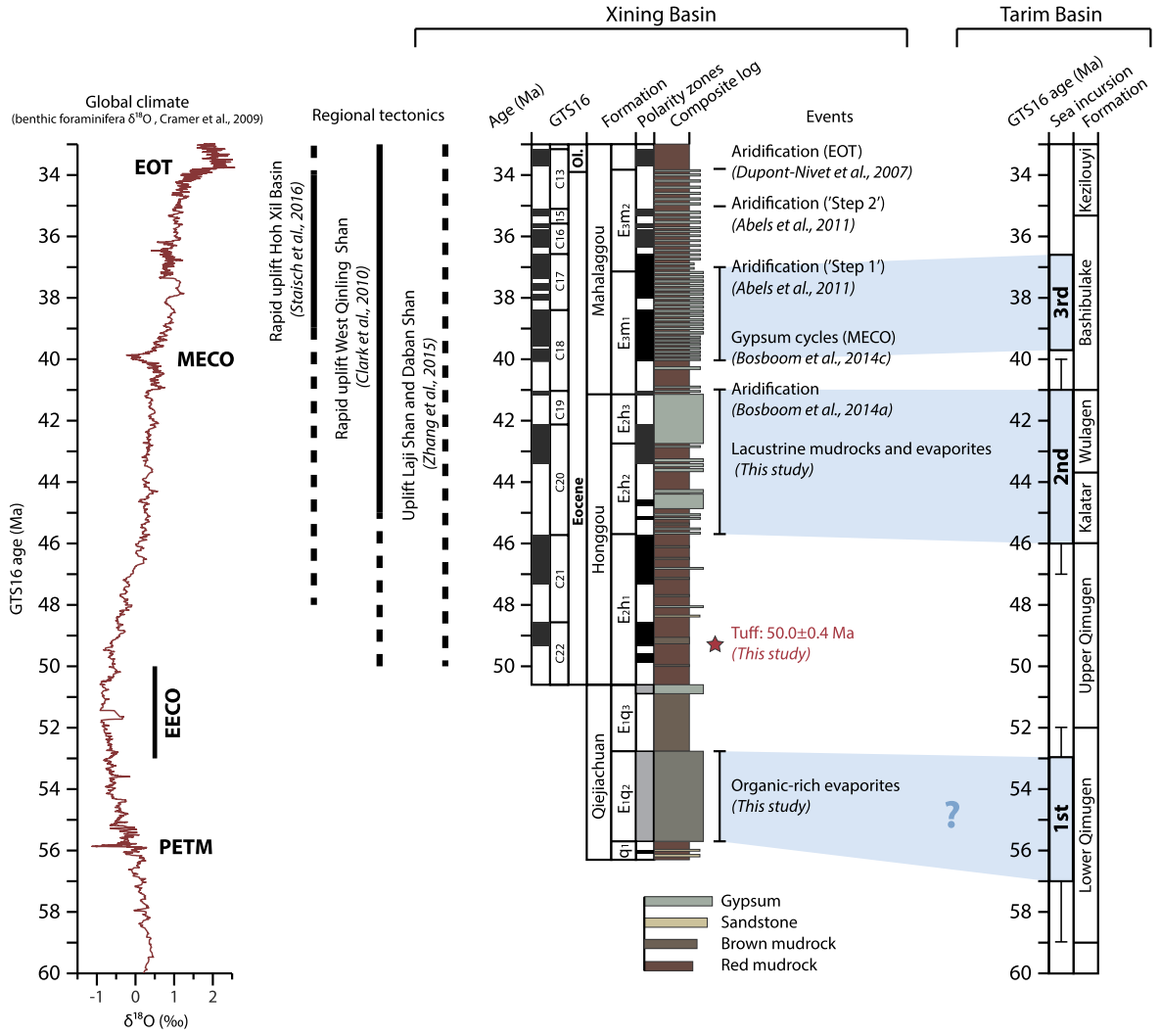

Fig. 6. Composite lithostratigraphy of the East Xining, Tiefo (Bosboom et al., 2014c) and Shuiwan (Abels et al., 2011) sections. Global climate is represented by a 9-point moving average through the benthic foraminifera δ18O record of Cramer et al. (2009). Regional tectonic events and climatic events observed in the basin are indicated, as well as the proto-Paratethys Sea incursions observed in the Tarim Basin (Kaya et al., 2018).

Within this long-term 50–34 Ma drying trend, we observed shorter term alternations between mudflat and saline lake deposits (Fig. 6). Based on previous interpretations in the Xining Basin, we interpret these alternations to represent fluctuations in atmospheric moisture (Dupont-Nivet et al., 2007, Abels et al., 2011). A first wet phase is expressed in the middle Qiejiachuan Formation by organic-rich evaporites. The age can only be approximated to late Paleocene–early Eocene based on existing pollen, ostracod and charophyte assemblages (Horton et al., 2004 and references therein) and by extending the average accumulation rate of the overlying deposits downwards. A second wet phase, is recognized as a shift to more

lacustrine mudrocks and evaporites in the middle to upper Honggou Formation. This phase can now be dated from ~46 Ma (top C21n) to the top of the upper Honggou evaporites as previously recognized at ~41 Ma (base of C18r; Bosboom et al., 2014a, Bosboom et al., 2014c). A third wet phase is observed to start at ~40 Ma (base C18n) with the onset of regular gypsum/mudrock cycles (Bosboom et al., 2014c) and end at a decrease in gypsum beds at ~37 Ma (top C17n.1n, 'Step 1' in Abels et al., 2011). This last phase was likely less intense, more fluctuating and drier, as indicated by the absence of organic-rich layers or carbonate beds and the presence of numerous interfingering layers of red mudrocks. These saline lake phases are laterally continuous throughout the basin suggesting an external control rather than an expression of autogenic basin infill. To identify potential driving mechanisms for the observed moisture fluctuations, we review constraints on tectonic uplift, proto-Paratethys Sea incursions and global climate trends (Fig. 6).

The influence of local tectonic uplift on moisture variations is considered unlikely because accumulation rates are continuously low (~3 cm/kyr, Fig. S5), no coarsening trends are observed and exhumation of the local mountain ranges (the Laji Shan and Daban Shan) occurred mainly in the Miocene (e.g. Lease et al., 2011). A loosely dated Eocene phase of exhumation is observed bordering the Xining Basin (Zhang et al., 2015) and more regionally in both the northern Tibetan Plateau (Western Qinling Shan; Clark et al., 2010) and the central Plateau (Hoh Xil Basin; Staisch et al., 2016). Although this Eocene growth of the Tibetan Plateau may explain the long-term drying trend (Li et al., 2018a), the observed shorter term shifts appear too abrupt (Fig. 3G) to be caused by the slow tectonic uplift of the Plateau. Furthermore, the continuously growing Plateau cannot explain the episodic occurrence of wetter lithofacies which are separated by intervals of dry mudflats.

Previous studies have temporally linked the Xining aridification steps to the stepwise retreating proto-Paratethys Sea (Dupont-Nivet et al., 2007, Abels et al., 2011; Bosboom et al., 2014a, Bosboom et al., 2014b). During the Paleogene, the long-term sea retreat is superimposed by three progressively smaller incursions each dated by bio- and magnetostratigraphic studies (Fig. 6, Fig. 7; Bosboom et al., 2014a, Bosboom et al., 2014b; Kaya et al., 2018). A recent reappraisal of these incursions in the Tarim Basin (Kaya et al., 2018) provides the following age constraints. The first and most extensive incursion lasted from ~59–57 Ma to ~53–52 Ma; the second incursion from ~47–46 Ma

to ~41–40 Ma and the third and smallest sea incursion is more precisely dated from 39.8 Ma to 36.7 Ma (Fig. 6, Fig. 7). These incursions fit well with the three wetter intervals recognized in the Xining Basin (Fig. 6). Our study therefore shows a temporal link between the proto-Paratethys highstands and increased moisture in the Xining Basin.

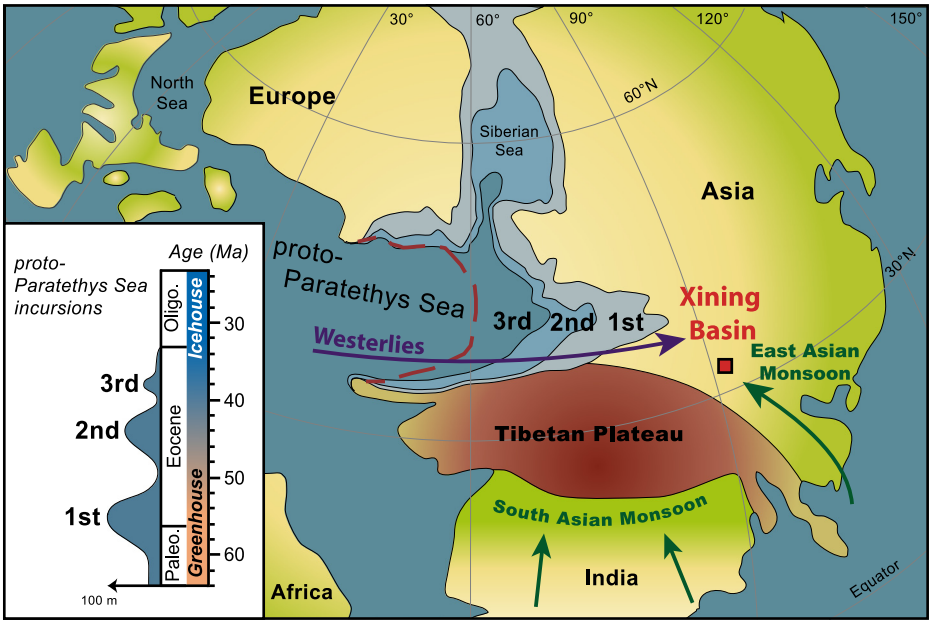

Fig. 7. Generalized paleogeography of Eurasia during the Paleogene, modified from Bosboom et al. (2014a). The maximum spatial extent of the three proto-Paratethys Sea incursions are indicated on the map and in time on the left. The approximate extent of the regressions in between the incursions is indicated with a red dashed line. Atmospheric moisture sources are shown with arrows.

This moisture could have been derived either from the winter-time westerlies or the summer monsoon (Fig. 7). Climate models suggest that Asian summer monsoons may be weakened by the proto-Paratethys Sea due to reduced land-sea contrasts (Ramstein et al., 1997, Zhang et al., 2007, Roe et al., 2016). Other studies indicate that the sea was too shallow to affect monsoonal circulation, even during highstands (Licht et al., 2014, Bougeois et al., 2018). Either way, it seems unlikely that an extensive proto-Paratethys Sea was associated with increased monsoonal activity. Instead, the highstands would increase the amount of water available for evaporation along the westerly pathway (Bosboom et al., 2014a, Bosboom et al., 2014b; Bougeois et al., 2018). This would result in more winter precipitation and provides an explanation for the wetter lithofacies in Xining coeval with the sea incursions. This interpretation is in line with previous studies showing that Central Asian climate and coeval deposits were

strongly influenced by the westerlies at this time (Caves et al., 2015, Bougeois et al., 2018).

Previous studies also suggested that global climate might have played a role in the Xining record (Fig. 6). Temperatures generally decreased during the studied interval but are superimposed by hyperthermal events and periods of incipient ice sheet formation (Fig. 6; e.g. Cramer et al., 2009). The onset of obliquity cycles after ~40 Ma has been associated with ice sheet dynamics after the MECO (Middle Eocene Climatic Optimum, Abels et al., 2011, Bosboom et al., 2014c) and the aridification at ~34 Ma has been linked to global cooling at the EOT (Dupont-Nivet et al., 2007). The latter may have resulted from either a weaker hydrological cycle in a colder climate (Licht et al., 2014, Li et al., 2018a), or from the proto-Paratethys Sea retreat induced by the growth of the Antarctic ice sheet (Dupont-Nivet et al., 2007, Bosboom et al., 2014a). However, the short-term moisture shifts observed in this study do not correspond with global climate events (Fig. 6). Instead, they systematically fit with the proto-Paratethys Sea incursions and retreats, some of which are thought to be driven by tectonics and others by eustasy (Bosboom et al., 2014a, Bosboom et al., 2014b; Kaya et al., 2018). Therefore, we suggest that the sea itself was a direct driver of precipitation in the region via the westerlies.

8. Conclusion

Our results extend the Xining record down to the early Eocene (~50 Ma) by using magnetostratigraphy and tuff dating. This extended time frame shows a long-term drying trend in the lithostratigraphy with superimposed wetter periods that correlate in time with highstands of the proto-Paratethys Sea. These correlations suggest that moisture in the region was governed by the westerlies and modulated by the Paleogene sea incursions. The overall aridification of the Xining Basin may be explained by the long-term retreat of the proto-Paratethys Sea as well as the effects of the Tibetan uplift and global cooling.

Our results stress that, beyond the traditionally invoked Tibetan uplift and global climate as drivers of Asian climate, sea-driven moisture fluctuations should be taken into account as well. These results might influence both the assessment of model and proxy data constraining Eurasian weathering and dust production (Licht et al., 2016) as well as paleobiogeographic reconstructions (e.g. Favre et al., 2015). Building upon these results, a better understanding of the interplay between the westerlies and monsoons at

tectonic, orbital and seasonal timescales may be obtained by further work focused on the identification and quantification of the moisture sources in the Xining Basin as well as in other regional records.

Acknowledgments

This work was funded by the ERC consolidator grant MAGIC 649081 to GDN. We thank Antje Musiol for support in the lab and we are grateful to Tianyuan Chen, Xiaohui Wu, Zhipeng Wu and Liu Xiang-Jun for field assistance and logistical support. We thank John Bershaw and two anonymous reviewers for their valuable comments.

References

H.A. Abels, G. Dupont-Nivet, G. Xiao, R. Bosboom, W. Krijgsman; Step-wise change of Asian interior climate preceding the Eocene–Oligocene Transition (EOT), Palaeogeogr. Palaeoclimatol. Palaeoecol., 299 (3) (2011), pp. 399-412, 10.1016/j.palaeo.2010.11.028

R. Bosboom, G. Dupont_Nivet, A. Grothe, H. Brinkhuis, G. Villa, O. Mandic, M. Stoica, W. H uang, W. Yang, Z. Guo, W. Krijgsman; Linking Tarim Basin sea retreat (west China) and Asian aridification in the late Eocene, Basin Res., 26 (5) (2014), pp. 621-640, 10.1111/bre.12054

R. Bosboom, G. Dupont_Nivet, A. Grothe, H. Brinkhuis, G. Villa, O. Mandic, M. Stoica, T. Ko uwenhoven, W. Huang, W. Yang, Z. GuoTiming, cause and impact of the late Eocene stepwise sea retreat from the Tarim Basin (west China) Palaeogeogr. Palaeoclimatol. Palaeoecol., 403 (2014), pp. 101-118, 10.1016/j.palaeo.2014.03.035

R.E. Bosboom, H.A. Abels, C. Hoorn, B.C. van den Berg, Z. Guo, G. Dupont-NivetAridification in continental Asia after the Middle Eocene Climatic Optimum (MECO); Earth Planet. Sci. Lett., 389 (2014), pp. 34-42, 10.1016/j.epsl.2013.12.014

L. Bougeois, G. Dupont-Nivet, M. de Rafélis, J.C. Tindall, J.N. Proust, G.J. Reichart, L.J. de Nooijer, Z. Guo, C. OrmukovAsian monsoons and aridification response to Paleogene sea retreat and Neogene westerly shielding indicated by seasonality in Paratethys oysters; Earth Planet. Sci. Lett., 485 (2018), pp. 99-110, 10.1016/j.epsl.2017.12.036

C. Bouligand, J. Dyment, Y. Gallet, G. HulotGeomagnetic field variations between chrons 33r and 19r (83–41 Ma) from sea-surface magnetic anomaly profiles; Earth Planet. Sci. Lett., 250 (3) (2006), pp. 541-560, 10.1016/j.epsl.2006.06.051

J.K. Caves, M.J. Winnick, S.A. Graham, D.J. Sjostrom, A. Mulch, C.P. ChamberlainRole of the westerlies in Central Asia climate over the Cenozoic; Earth Planet. Sci. Lett., 428 (2015), pp. 33-43, 10.1016/j.epsl.2015.07.023

J.B. Chapman, P. KappTibetan magmatism database; Geochem. Geophys. Geosyst (2017), 10.1002/2017GC007217

M.K. Clark, K.A. Farley, D. Zheng, Z. Wang, A.R. DuvallEarly Cenozoic faulting of the northern Tibetan Plateau margin from apatite (U–Th)/He ages; Earth Planet. Sci. Lett., 296 (1) (2010), pp. 78-88, 10.1016/j.epsl.2010.04.051

B.S. Cramer, J.R. Toggweiler, J.D. Wright, M.E. Katz, K.G. MillerOcean overturning since the Late Cretaceous: inferences from a new benthic foraminiferal isotope compilation; Paleoceanography, 24 (4) (2009), 10.1029/2008PA001683

S. Dai, X. Fang, G. Dupont-Nivet, C. Song, J. Gao, W. Krijgsman, C. Langereis, W. ZhangMagnetostratigraphy of Cenozoic sediments from the Xining Basin: tectonic implications for the northeastern Tibetan Plateau; J. Geophys. Res., Solid Earth, 111 (B11) (2006), 10.1029/2005JB004187

G. Dupont-Nivet, W. Krijgsman, C.G. Langereis, H.A. Abels, S. Dai, X. FangTibetan plateau aridification linked to global cooling at the Eocene–Oligocene transition; Nature, 445 (7128) (2007), pp. 635-638

G. Dupont-Nivet, C. Hoorn, M. KonertTibetan uplift prior to the Eocene–Oligocene climate transition: evidence from pollen analysis of the Xining Basin; Geology, 36 (12) (2008), pp. 987-990, 10.1130/G25063A.1

G. Dupont-Nivet, S. Dai, X. Fang, W. Krijgsman, V. Erens, M. Reitsma, C. LangereisTiming and distribution of tectonic rotations in the northeastern Tibetan Plateau; Investigations into the Tectonics of the Tibetan Plateau, Geological Society of America, Special Papers, vol. 444 (2008), pp. 73-87

X. Fang, J. Zan, E. Appel, Y. Lu, C. Song, S. Dai, S. TuoAn Eocene–Miocene continuous rock magnetic record from the sediments in the Xining Basin, NW China: indication for Cenozoic persistent drying driven by global cooling and Tibetan Plateau uplift; Geophys. J. Int., 201 (1) (2015), pp. 78-89, 10.1093/gji/ggv002

A. Favre, M. Päckert, S.U. Pauls, S.C. Jähnig, D. Uhl, I. Michalak, A.N. Muellner-RiehlThe role of the uplift of the Qinghai–Tibetan Plateau for the evolution of Tibetan biotas; Biol. Rev., 90 (1) (2015), pp. 236-253, 10.1111/brv.12107

R. FisherDispersion on a sphere; Proc. R. Soc. Lond. A, Math. Phys. Eng. Sci., 217 (1130) (1953, May), pp. 295-305, 10.1098/rspa.1953.0064

Z.T. Guo, B. Sun, Z.S. Zhang, S.Z. Peng, G.Q. Xiao, J.Y. Ge, Q.Z. Hao, Y.S. Qiao, M.Y. Liang, J.F. Liu, Q.Z. Yin, J. WeiA major reorganization of Asian climate by the early Miocene; Clim. Past, 4 (3) (2008), pp. 153-174, 10.5194/cp-4-153-2008

B.K. Horton, G. Dupont-Nivet, J. Zhou, G.L. Waanders, R.F. Butler, J. WangMesozoic–Cenozoic evolution of the Xining–Minhe and Dangchang basins, northeastern Tibetan Plateau: magnetostratigraphic and biostratigraphic results; J. Geophys. Res., Solid Earth, 109 (B4) (2004), 10.1029/2003JB002913

M. Huber, A. GoldnerEocene monsoons; J. Asian Earth Sci., 44 (2012), pp. 3-23, 10.1016/j.jseaes.2011.09.014

M.Y. Kaya, G. Dupont-Nivet, J-N. Proust, P. Roperch, L. Bougeois, N. Meijer, J. Frieling, C. Fioroni, S.Ö. Altiner, E. Vardar, M. Stoica, M. Mamtimin, Z. GuoPaleogene evolution and demise of the proto-Paratethys Sea in Central Asia (Tarim and Tajik basins): role of intensified tectonic activity at ~41 Ma; Basin Res (2018), 10.1111/bre.12330

J.L. KirschvinkThe least-squares line and plane and the analysis of palaeomagnetic data; Geophys. J. Int., 62 (3) (1980), pp. 699-718, 10.1111/j.1365-246X.1980.tb02601.x

R.O. Lease, D.W. Burbank, M.K. Clark, K.A. Farley, D. Zheng, H. ZhangMiddle Miocene reorganization of deformation along the northeastern Tibetan Plateau; Geology, 39 (4) (2011), pp. 359-362, 10.1130/G31356.1

R.W. Le Maitre, P. Bateman, A. Dudek, J. Keller, J. Lameyre, M. Le Bas, P. Sabine, R. Schmid, H. Sorensen, A. Streckeisen, A.R. Woolley, B. ZanettinA Classification of Igneous Rocks and Glossary of Terms: Recommendations of the International Union of Geological Sciences, Subcommission on the Systematics of Igneous Rocks; Blackwell, Oxford (1989); 193 pp

X. Li, R. Zhang, Z. Zhang, Q. YanWhat enhanced the aridity in Eocene Asian inland: global cooling or early Tibetan Plateau uplift?; Palaeogeogr. Palaeoclimatol. Palaeoecol., 510 (2017), pp. 6-14, 10.1016/j.palaeo.2017.10.029

X. Li, R. Zhang, Z. Zhang, Q. YanDo climate simulations support the existence of East Asian monsoon climate in the Late Eocene?; Palaeogeogr. Palaeoclimatol. Palaeoecol., 509 (2018), pp. 47-57, 10.1016/j.palaeo.2017.12.037

A. Licht, M. Van Cappelle, H.A. Abels, J.B. Ladant, J. Trabucho-Alexandre, C. France-Lanord, Y. Donnadieu, J. Vandenberghe, T. Rigaudier, C. Lécuyer, D. Terry Jr., R. A driaens, A. Boura, Z. Guo, Soe Aung Naing, J. Quade, G. Dupont-Nivet, J.-J. JaegerAsian monsoons in a late Eocene greenhouse world; Nature, 513 (7519) (2014), pp. 501-506

A. Licht, G. Dupont-Nivet, A. Pullen, P. Kapp, H.A. Abels, Z. Lai, Z. Guo, J. Abell, D. GieslerResilience of the Asian atmospheric circulation shown by Paleogene dust provenance; Nat. Commun., 7 (2016), Article 12390

K.R. Ludwig, R. MundilExtracting reliable U–Pb ages and errors from complex populations of zircons from Phanerozoic tuffs; Goldschmidt Conference Abstracts 2002 (2002); A453

P.L. McFadden, M.W. McElhinnyClassification of the reversal test in palaeomagnetism; Geophys. J. Int., 103 (3) (1990), pp. 725-729, 10.1111/j.1365-246X.1990.tb05683.x

P. Molnar, W.R. Boos, D.S. BattistiOrographic controls on climate and paleoclimate of Asia: thermal and mechanical roles for the Tibetan Plateau; Annu. Rev. Earth Planet. Sci., 38 (2010), 10.1146/annurev-earth-040809-152456

C.P. North, S.K. DavidsonUnconfined alluvial flow processes: recognition and interpretation of their deposits, and the significance for palaeogeographic reconstruction; Earth-Sci. Rev., 111 (1) (2012), pp. 199-223, 10.1016/j.earscirev.2011.11.008

J.G. Ogg, G. Ogg, F.M. GradsteinA Concise Geologic Time Scale: 2016; Elsevier (2016)

P.E. Potter, J.B. Maynard, P.J. DepetrisMud and Mudstones: Introduction and Overview; Springer Science & Business Media (2005)

Qinghai Bureau of Geology and Mineral Resources (QBGMR)Geologic Maps of the Duoba, Gaodian, Tianjiazai, and Xining Regions (4 Sheets), with Regional Geologic Report (1:50,000 Scale); (1985); Xining, China, 199 pp

C. Quan, Z. Liu, T. Utescher, J. Jin, J. Shu, Y. Li, Y.S.C. LiuRevisiting the Paleogene climate pattern of East Asia: a synthetic review; Earth-Sci. Rev., 139 (2014), pp. 213-230, 10.1016/j.earscirev.2014.09.005

G. Ramstein, F. Fluteau, J. Besse, S. JoussaumeEffect of orogeny, plate motion and land-sea distribution on Eurasian climate change over the past 30 million years; Nature, 386 (6627) (1997), pp. 788-795

G.H. Roe, Q. Ding, D.S. Battisti, P. Molnar, M.K. Clark, C.N. GarzioneA modeling study of the response of Asian summertime climate to the largest geologic forcings of the past 50 Ma; J. Geophys. Res., Atmos., 121 (10) (2016), pp. 5453-5470, 10.1002/2015JD024370

M.R. RosenThe importance of groundwater in playas: a review of playa classifications and; Paleoclimate and Basin Evolution of Playa Systems, Geological Society of America, Special Papers, vol. 289 (1994), p. 1

J.P. Smoot, T.K. LowensteinDepositional environments of non-marine evaporites; Developments in Sedimentology, vol. 50, Elsevier (1991), pp. 189-347, 10.1016/S0070-4571(08)70261-9

Spicer et al., 2017;

R. Spicer, J. Yang, A. Herman, T. Kodrul, G. Aleksandrova, N. Maslova, T. Spicer, L. Ding, Q. Xu, A. Shukla, G. Srivastava, R. Mehrotra, X.-Y. Liu, J.-H. JinPaleogene monsoons across India and South China: drivers of biotic change; Gondwana Res., 49 (2017), pp. 350-363, 10.1016/j.gr.2017.06.006

J.S. Stacey, J.D. KramerApproximation of terrestrial lead isotope evolution by a two stage model; Earth Planet. Sci. Lett., 26 (1975), pp. 207-221, 10.1016/0012-821X(75)90088-6

L.M. Staisch, N.A. Niemi, M.K. Clark, H. ChangEocene to late Oligocene history of crustal shortening within the Hoh Xil Basin and implications for the uplift history of the northern Tibetan Plateau; Tectonics, 35 (4) (2016), pp. 862-895, 10.1002/2015TC003972

M.R. Talbot, K. Holm, M.A.J. WilliamsSedimentation in low-gradient desert margin systems: a comparison of the Late Triassic of northwest Somerset (England) and the late Quaternary of east-central Australia; Paleoclimate and Basin Evolution of Playa Systems, Geological Society of America, Special Papers, vol. 289 (1994), pp. 97-117

A. Turtù, V. Lauretano, R. Catanzariti, F.J. Hilgen, S. Galeotti, L. Lanci, M. Moretti, L.J. Lour ensIntegrated stratigraphy of the Smirra Core (Umbria–Marche Basin, Apennines, Italy): a new early Paleogene reference section and implications for the geologic time scale; Palaeogeogr. Palaeoclimatol. Palaeoecol., 487 (2017), pp. 158-174, 10.1016/j.palaeo.2017.08.031

T. Westerhold, U. Röhl, T. Frederichs, C. Agnini, I. Raffi, J.C. Zachos, R.H. WilkensAstrono mical calibration of the Ypresian timescale: implications for seafloor spreading rates and the chaotic behavior of the solar system?; Clim. Past, 13 (9) (2017), p. 1129, 10.5194/cp-13-1129-2017

G. Xiao, Z. Guo, G. Dupont-

Nivet, H. Lu, N. Wu, J. Ge, Q. Hao, S. Peng, F. Li, H.A. Abels, K. ZhangEvidence for northeastern Tibetan Plateau uplift between 25 and 20 Ma in the sedimentary archive of the Xining Basin, Northwestern China; Earth Planet. Sci. Lett., 317 (2012), pp. 185-195, 10.1016/j.epsl.2011.11.008

Z. Zhang, H. Wang, Z. Guo, D. JiangWhat triggers the transition of palaeoenvironmental patterns in China, the Tibetan Plateau uplift or the Paratethys Sea retreat?; Palaeogeogr. Palaeoclimatol. Palaeoecol., 245 (3–4) (2007), pp. 317-331, 10.1016/j.palaeo.2006.08.003

J. Zhang, Y. Wang, B. Zhang, H. ZhaoEvolution of the NE Qinghai–Tibetan Plateau, constrained by the apatite fission track ages of the mountain ranges around the Xining Basin in NW China, J. Asian Earth Sci., 97 (2015), pp. 10-23, 10.1016/j.jseaes.2014.10.002

J. Zhang, Y. Wang, B. Zhang, Y. ZhangTectonics of the Xining Basin in NW China and its implications for the evolution of the NE Qinghai–Tibetan Plateau, Basin Res., 28 (2) (2016), pp. 159-182, 10.1111/bre.12104

The following is the Supplementary material related to this article.

MMC 1. Supplementary material: Analytical procedure for U–Pb geochronology.

Fig. S1. Studied sections showing: a) detailed lithological logs of the studied sections. b) Virtual Geomagnetic Pole (VGP) latitudes and corresponding polarity zones.

Fig. S2. Total alkali-silica (TAS) diagram (Le Maitre et al., 1989) of the tuff layers (A, B and C in Fig. 3G) classifying the tuff as trachyte.

Fig. S3. Thermal demagnetization of representative samples shown in vector end point diagrams on the left (numbers indicate temperature steps) and remanent magnetizationon the right. (a) Normal polarity in N3 (Caija, 71.5 m). (b) Reversed polarity in R1 (Xiejia, 15.3 m). (c) Normal polarity in N5 (Caijia, 188.5 m). (d) Normal polarity in N2 (Xiejia, 29.1 m). The samples shown in (c) and (d) are from normal polarity zones that were not correlated to the GTS.

Fig. S4. Equal-area stereographic projections in the lower hemisphere of the ChRMs calculated in the different sections. The ChRMs are shown both in situ (IS) and tilt-corrected (TC). Samples removed after 45° cutoff are indicated in red and samples from normal polarity zones that are not correlated to the GTS are indicated in blue.

Fig. S5. Sediment accumulation rates for the different magnetostratigraphic sections correlated to the GTS16 (Ogg et al., 2016). Rates are shown in cm/kyr.

Table S1. Geochemical analyses of major (%) and minor (ppm) elements of the three layers within the tuff bed (A, B and C).

Table S2. Operating conditions for the LA-ICP-MS equipment.

Table S3. U–Pb data for the 31 analyzed zircon grains. All errors are listed at 1σ. Data in bold were used for the tuff age calculation (% conc. = Percentage of concordance).

Data 1. U–Pb Pleso standards.

Data 2. Magnetostratigraphy.

Supplementary material:

Analytical procedure for U-Pb geochronology

U-Pb geochronology was conducted by in-situ laser ablation inductively coupled plasma mass spectrometry (LA-ICPMS) at Géosciences Rennes using an ESI NWR193UC excimer laser coupled to a quadripole Agilent 7700x ICP-MS equipped with a dual pumping system to enhance sensitivity (Paquette et al. 2014). The instrumental conditions are reported in Table S2.

The ablated material is carried into helium, and then mixed with nitrogen and argon, before being injected into the plasma source. The alignment of the instrument and mass calibration was performed before the analytical session using the NIST SRM 612 reference glass, by inspecting the ^{238}U signal and by minimizing the ThO+/Th+ ratio (<0.5%). During the course of an analysis, the signals of ^{204}(Pb+Hg), ^{206}Pb, ^{207}Pb, ^{208}Pb and ^{238}U masses are acquired. The ^{235}U signal is calculated from ^{238}U on the basis of the ratio ^{238}U /^{235}U =137.88.

Single analyses consisted of 20 seconds of background integration followed by 60 seconds integration with the laser firing and then a 15 seconds delay to wash out the previous sample. The ESI NWR193UC laser is equipped with a rotational XY shutter, which allows rectangular ablations while ensuring an even “dosage” of the laser energy to the sample during the analyses. Because the zircon grains of the tuff sample are very elongated and narrow, we defined a rectangle of 70x20 mm that was suitable for most of the grains in this sample. This ablation rectangle, which can rotate freely around its center, was then used for all the standards and the zircon crystals in order to use the same analytical conditions during the analyses.

The data were corrected for U–Pb fractionation and for mass bias by repeated measurements of the Gj1 zircon standard (Jackson et al., 2004). The six Plešovice zircon standard (Sláma et al., 2008) measurements were treated as unknowns and were used to control the reproducibility and accuracy of the corrections. During the course of the analyses, they provided a Concordia age of 337.7 ± 3.1 Ma (MSWD=0.15, probability=0.999). Data reduction was carried out with the Glitter Software (van Achterbergh et al., 2001). Concordia ages and diagrams were generated using Isoplot/Ex (Ludwig, 2001). All errors given in the data tables are listed at one sigma, but where data are combined for regression analysis, the final results are provided with 95% confidence limits. Further information on the protocol can be found in Ballouard et al. (2015).

Figure and table captions

Fig. S1 Studied sections showing: a) detailed lithological logs of the studied sections. b) Virtual Geomagnetic Pole (VGP) latitudes and corresponding polarity zones.

Fig. S2 Total alkali-silica (TAS) diagram (Le Maitre et al., 1989) of the tuff layers (A, B and C in Fig. 3g) classifying the tuff as trachyte.

Fig. S3 Thermal demagnetization of representative samples shown in vector end point diagrams on the left (numbers indicate temperature steps) and remanent magnetization on the right. (a) Normal polarity in N3 (Caija, 71.5 meter). (b) Reversed polarity in R1 (Xiejia, 15.3 meter). (c) Normal polarity in N5 (Caijia, 188.5 meter). (d) Normal polarity in N2 (Xiejia, 29.1 meter). The samples shown in (c) and (d) are from normal polarity zones that were not correlated to the GTS.

Fig. S4 Equal-area stereographic projections in the lower hemisphere of the ChRMs calculated in the different sections. The ChRMs are shown both in situ (IS) and tilt-corrected (TC). Samples removed after 45° cutoff are indicated in red and samples from normal polarity zones that are not correlated to the GTS are indicated in blue.

Fig. S5 Sediment accumulation rates for the different magnetostratigraphic sections correlated to the GTS16 (Ogg et al., 2016). Rates are shown in cm/kyr.

Table S1: Geochemical analyses of major (%) and minor (ppm) elements of the three layers within the tuff bed (A, B and C).

Table S2: Operating conditions for the LA-ICP-MS equipment.

TableS3: U-Pb data for the 31 analyzed zircon grains. All errors are listed at 1σ. Data in bold were used for the tuff age calculation (%conc. = Percentage of concordance).

Data1 U-Pb Pleso standards

Data2 Magnetostratigraphy

Supplementary references:

Ballouard, C., Boulvais, P., Poujol, M., Gapais, D., Yamato, P., Tartèse, R., and Cuney, M., (2015), Tectonic record, magmatic history and hydrothermal alteration in the Hercynian Guérande leucogranite, Armorican Massif, France: *Lithos, v. 220-223*, p. 1-22. https://doi.org/10.1016/j.lithos.2015.01.027

Jackson SE, Pearson NJ, Griffin WL, Belousova EA (2004) The application of laser-ablation-inductively coupled plasma-mass spectrometry to in situ U-Pb zircon geochronology. *Chemical Geology 211*:47-69. https://doi.org/10.1016/j.chemgeo.2004.06.017

Le Maitre, R. W., Bateman, P., Dudek, A., Keller, J., Lameyre, J., Le Bas, M., Sabine, P., Schmid, R., Sorensen, H., Streckeisen, A., Woolley, A. R. & Zanettin, B. (1989). A classification of igneous rocks and glossary of terms: Recommendations of the International Union of Geological Sciences, Subcommission on the Systematics of Igneous Rocks. *Blackwell Oxford* (193 pp).

Ludwig, K.R. (2001). Isoplot/Ex Version 2.49. A Geochronological Toolkit for Microsoft Excel. *Berkeley Geochronology Center, Special, Publication 1app*. 1–55.

Ogg, J. G., Ogg, G., & Gradstein, F. M. (2016). A concise geologic time scale: 2016. Elsevier.

Paquette, J.-L., Piro, J.-L., Devidal, J.-L., Bosse, V., Didier, A., Sanac, S., and Abdelnour, Y. (2014). Sensitivity enhancement in LA-ICP-MS by N2 addition to carrier gas: Application to radiometric dating of U-Th-bearing minerals: *Agilent ICP-MS Journal, v. 58*, p. 1-5.

Sláma, J., Kosler, D., Condon, D.J., Crowley, J.L., Gerdes, A., Hanchar, J.M., Horstwood,M.S.A., Morris, G.A., Nasdala, L., Norberg, N., Schaltegger, U., Schoene, B., Tubrett, M.N., Whitehouse, M.J. (2008). Plesovice zircon — a new natural reference material for U–Pb and Hf isotopic microanalysis. *Chem. Geol. 249*, 1–35. https://doi.org/10.1016/j.chemgeo.2007.11.005

Van Achterbergh, E., Ryan, C. G., Jackson, S. E., and Griffin, W. L. (2001). Data reduction software for LA-ICP-MS: appendix, in Sylvester, P. J., ed., *Laser Ablation-ICP-Mass Spectrometry in the Earth Sciences: Principles and Applications, Volume 29: Ottawa, Ontario, Canada, Mineralog. Assoc. Canada (MAC),* p. 239-243.

East Xining

a) Lithostratigraphy

b) Magnetostratigraphy

Stratigraphic position (m)

E_3m_1

E_2h_3

E_2h_2

E_2h_1

E_1q_3

E_1q_2

E_1q_1

clayst. siltst. v. fine sst.

-90°S 0 90°N

VGP latitude

Caijia

a) Lithostratigraphy

b) Magnetostratigraphy

E_2h_2

E_2h_1

E_1q_3

clayst. siltst. v. fine sst.

-90°S 0 90°N

VGP latitude

Xiejia

a) Lithostratigraphy

b) Magnetostratigraphy

h_3

E_2h_2

E_2h_1

E_1q_3

Tuff:
50.0±0.4 Ma

clayst. siltst. v. fine sst.

-90°S 0 90°N

VGP latitude

Legend Magnetostratigraphy

- VGP
- Rejected VGP
- Normal polarity
- Reversed polarity
- Uncertain polarity
- No data

Legend Lithostratigraphy

- Gypsum
- Limestone
- Sandstone
- Mudrock
- Fault
- Ripple lamination
- Horizontal lamination
- Slickensides
- Burrows
- Mudcracks
- Mottling
- Organic material
- Rootlets
- Carbonate nodules
- Gypsum nodules

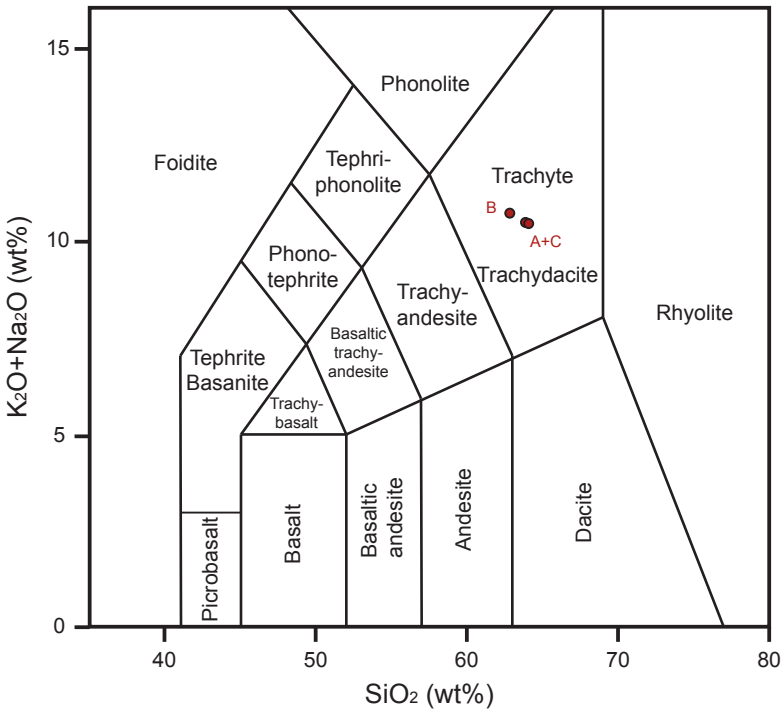
15
10
5
0
40
50
60
70
80
K_2O+Na_2O (wt%)
SiO_2 (wt%)
Phonolite
Foidite
Tephri-
phonolite
Trachyte
B
A+C
Phono-
tephrite
Trachydacite
Trachy-
andesite
Rhyolite
Basaltic
trachy-
andesite
Tephrite
Basanite
Trachy-
basalt
Picrobasalt
Basalt
Basaltic
andesite
Andesite
Dacite

Horizontal component

Vertical component

Thermal demagnetization:

A) Normal polarity (N3)

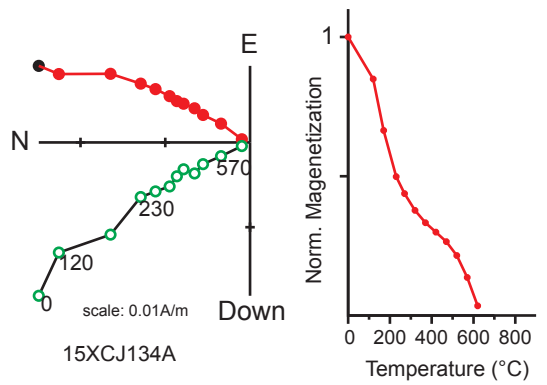

B) Reversed polarity (R1)

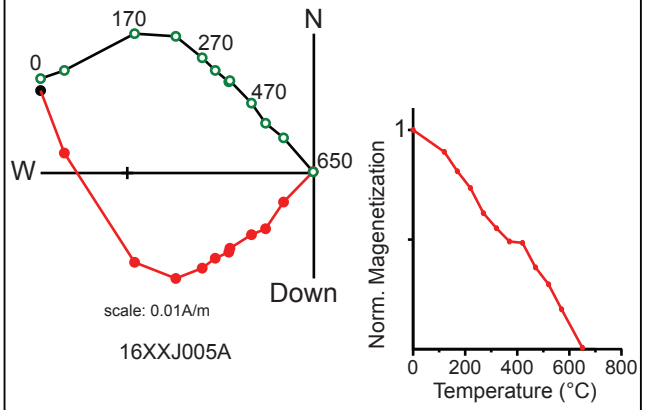

C) Uncorrelated normal polarity zone (N5)

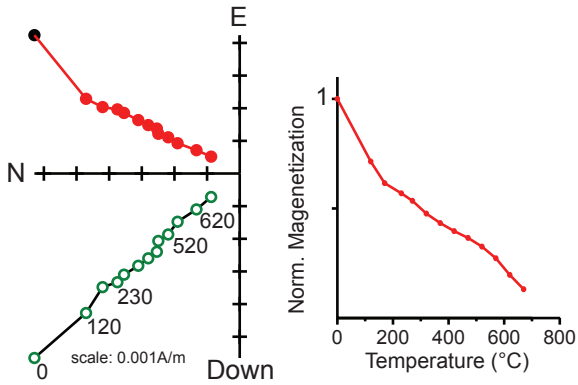

D) Uncorrelated normal polarity zone (N2)

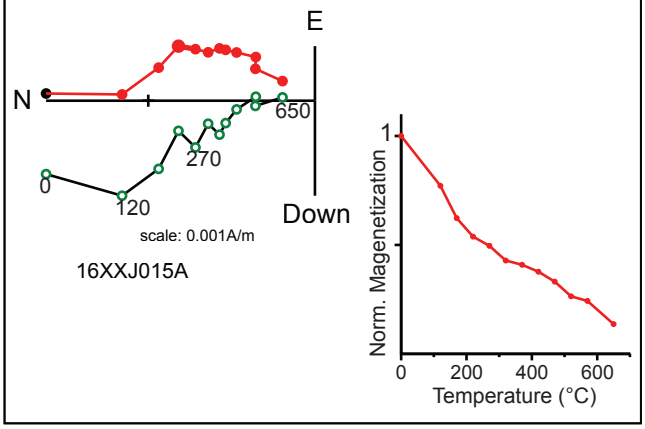

East Xining

Normal (TC): D = 3.9°; I = 39.7° ; α95 = 5.0°; n = 88
Reversed (TC): D = 208.8°; I = -40.8° ; α95 = 4.3°; n = 127

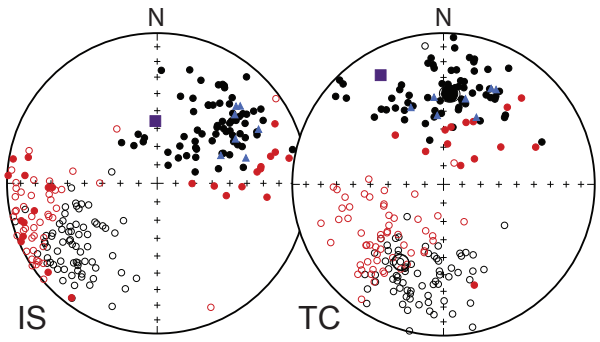

Caijia

Normal (TC): D = 22.8°; I = 36.3° ; α95 = 4.3°; n = 108
Reversed (TC): D = 206.6°; I = -35.1° ; α95 = 2.7°; n = 225

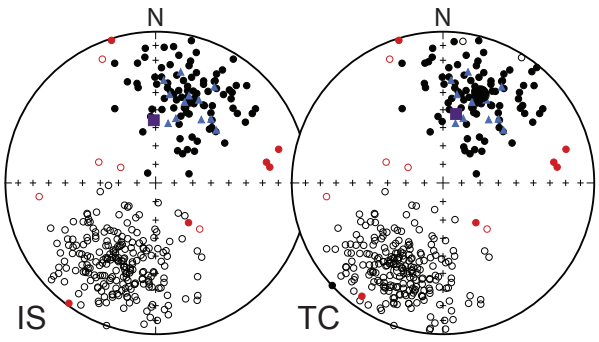

Xiejia

Normal (TC): D = 16.1°; I = 31.2° ; α95 = 6.0°; n = 71
Reversed (TC): D = 218.3°; I = -37.3° ; α95 = 5.8°; n = 101

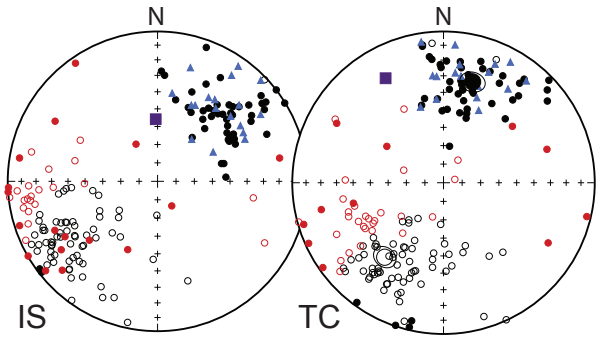

Legend

- Present day normal
- Directions
- Rejected directions after 45 cutoff
- Directions of uncorrelated normal chrons

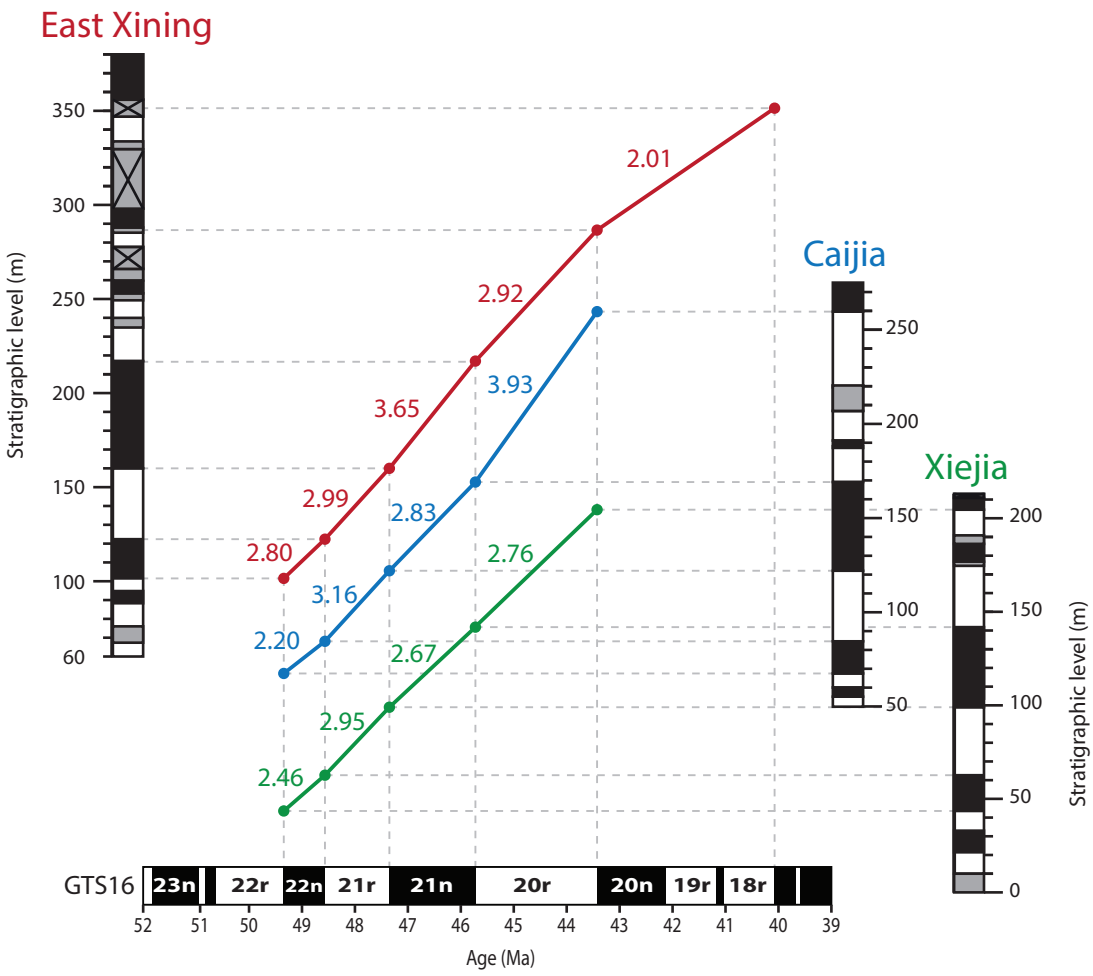
East Xining
Caijia
Xiejia
Stratigraphic level (m)
Stratigraphic level (m)
350
300
250
200
150
100
60
250
200
150
100
50
200
150
100
50
0
2.01
2.92
3.65
2.99
2.80
3.93
2.83
3.16
2.20
2.76
2.67
2.95
2.46
GTS16
23n
22r
22n
21r
21n
20r
20n
19r
18r
52
51
50
49
48
47
46
45
44
43
42
41
40
39
Age (Ma)

Sample #	SiO_2 (%)	TiO_2 (%)	Al_2O_3 (%)	Fe_2O_3 (%)	MnO (%)	MgO (%)	CaO (%)	Na_2O (%)	K_2O (%)	P_2O_5 (%)	LOI (%)	Sum (%)
XJTUFF C	58.47	0.35	18.51	1.19	0.06	0.87	2.37	8.87	0.74	0.10	8.14	99.67
XJTUFF B	56.88	0.33	18.37	0.90	0.09	0.76	3.37	9.10	0.62	0.09	9.28	99.79
XJTUFF A	58.80	0.37	18.88	1.31	0.05	0.96	1.67	8.75	0.86	0.10	8.15	99.90
Sample #	Ba (ppm)	Cr (ppm)	Ga (ppm)	Nb (ppm)	Ni (ppm)	Rb (ppm)	Sr (ppm)	V (ppm)	Y (ppm)	Zn (ppm)	Zr (ppm)	Sum (ppm)
XJTUFF C	338	35	14	25	19	51	185	102	20	15	106	910
XJTUFF B	325	17	16	26	13	41	277	44	24	24	89	896
XJTUFF A	338	37	15	25	18	49	206	64	21	30	100	903

Laboratory & Sample Preparation	
Laboratory name	Géosciences Rennes, UMR CNRS 6118, Rennes, France
Sample type/mineral	Detrital and magmatic zircon grains
Sample preparation	Conventional mineral separation, 1 inch resin mount, 1mm polish to finish
Imaging	CL: RELION CL instrument, Olympus Microscope BX51WI, Leica Color Camera DFC 420C
Laser ablation system	
Make, Model & type	ESI NWR193UC, Excimer
Ablation cell	ESI NWR TwoVol2
Laser wavelength	193 nm
Pulse width	< 5 ns
Fluence	8.0 J/cm^2
Repetition rate	3 Hz
Spot size	20x70 µm (rotational XY shutter)
Sampling mode / pattern	Single spot

Carrier gas	100% He, Ar make-up gas and N2 (3 ml/mn) combined using in-house smoothing device
Background collection	20 seconds
Ablation duration	60 seconds
Wash-out delay	15 seconds
Cell carrier gas flow (He)	0.72 l/min
ICP-MS Instrument	
Make, Model & type	Agilent 7700x, Q-ICP-MS
Sample introduction	Via conventional tubing
RF power	1350W
Sampler, skimmer cones	Ni
Extraction lenses	X type
Make-up gas flow (Ar)	0.81 l/min
Detection system	Single collector secondary electron multiplier
Data acquisition protocol	Time-resolved analysis
Scanning mode	Peak hopping, one point per peak

Detector mode	Pulse counting, dead time correction applied, and analog mode when signal intensity > ~ 10^6 cps
Masses measured	^{204}(Hg + Pb), ^{206}Pb, ^{207}Pb, ^{208}Pb, ^{232}Th, ^{238}U
Integration time per peak	10-30 ms
Sensitivity / Efficiency	24000 cps/ppm Pb (50µm, 10Hz)
Data Processing	
Gas blank	20 seconds on-peak
Calibration strategy	GJ1 zircon standard used as primary reference material, Plešovice used as secondary reference material (quality control)
Reference Material info	GJ1 (Jackson et al., 2004) Plešovice (Slama et al., 2008)
Data processing package used	GLITTER ® (van Achterbergh et al., 2001)
Quality control / Validation	Plešovice: concordia age = 337.7 ± 3.1 Ma (N=6; MSWD=0.15; probability=0.999)

					Isotopic ratios				Apparent Ages				
Grain number	Pb (ppm)	U (ppm)	Th (ppm)	Th/U	238U/206Pb	Error (%)	207Pb/206Pb	Error (%)	206Pb/238U	Abs.Err	207Pb/235U	Abs.Err	% Conc.
Zr1	95	1559	343	0.2	17.33	1.16	0.1053	1.02	362	4	618	5	59
Zr3	97	163	145	0.9	2.111	1.17	0.1753	1.01	2500	24	2560	11	98
Zr5	**9**	**986**	**823**	**0.8**	**128.4**	**1.16**	**0.0486**	**1.28**	**50.0**	**0.6**	**51.6**	**0.7**	**97**
Zr7	128	1093	283	0.3	9.04	1.17	0.1057	1.01	676	8	975	7	69
Zr9	32	219	120	0.5	7.363	1.17	0.0670	1.03	821	9	825	7	99
Zr10	**3**	**346**	**195**	**0.6**	**127.6**	**1.15**	**0.0506**	**1.62**	**50.3**	**0.6**	**54**	**0.9**	**93**
Zr11	**4**	**503**	**387**	**0.8**	**127.2**	**1.15**	**0.0496**	**1.53**	**50.5**	**0.6**	**53.1**	**0.84**	**95**
Zr13	**7**	**744**	**687**	**0.9**	**129.5**	**1.17**	**0.0489**	**1.60**	**49.6**	**0.6**	**51.5**	**0.84**	**96**
Zr14	**7**	**832**	**802**	**1.0**	**131.8**	**1.19**	**0.0512**	**1.23**	**48.7**	**0.6**	**53**	**0.7**	**92**
Zr16	**9**	**999**	**797**	**0.8**	**128.0**	**1.15**	**0.0482**	**1.39**	**50.1**	**0.6**	**51.3**	**0.75**	**98**
Zr17	**4**	**433**	**310**	**0.7**	**127.9**	**1.15**	**0.0476**	**1.57**	**50.2**	**0.6**	**50.9**	**0.83**	**99**
Zr18	**4**	**492**	**278**	**0.6**	**125.8**	**1.26**	**0.0501**	**1.46**	**51.1**	**0.6**	**54.4**	**0.83**	**94**
Zr20	**5**	**550**	**457**	**0.8**	**128.4**	**1.16**	**0.0501**	**1.34**	**50.0**	**0.6**	**53.2**	**0.76**	**94**
Zr21	11	228	108	0.5	21.03	1.18	0.0633	1.12	300	3	352	4	85
Zr22	9	146	148	1.0	20.46	1.19	0.0595	1.18	308	4	342	4	90
Zr27	**6**	**632**	**471**	**0.7**	**128.9**	**1.16**	**0.0540**	**1.32**	**49.8**	**0.6**	**57**	**0.79**	**87**
zr28	**4**	**465**	**197**	**0.4**	**125.0**	**1.25**	**0.0502**	**2.95**	**51.4**	**0.7**	**54.7**	**1.57**	**94**
Zr29	**7**	**818**	**646**	**0.8**	**129.4**	**1.16**	**0.0524**	**1.35**	**49.6**	**0.6**	**55.2**	**0.78**	**90**
Zr31	**6**	**607**	**527**	**0.9**	**123.9**	**1.24**	**0.0491**	**1.53**	**51.8**	**0.6**	**54.1**	**0.84**	**96**
Zr34	**5**	**525**	**365**	**0.7**	**129.4**	**1.16**	**0.0502**	**1.75**	**49.6**	**0.6**	**52.9**	**0.94**	**94**
Zr36	**5**	**502**	**373**	**0.7**	**129.2**	**1.16**	**0.0535**	**1.53**	**49.7**	**0.6**	**56.4**	**0.89**	**88**
Zr38	**9**	**904**	**850**	**0.9**	**124.8**	**1.12**	**0.0474**	**1.24**	**51.5**	**0.6**	**51.8**	**0.69**	**99**
Zr39	**6**	**706**	**544**	**0.8**	**130.9**	**1.18**	**0.0487**	**1.58**	**49.1**	**0.6**	**50.8**	**0.83**	**97**
Zr40	11	98	88	0.9	10.35	1.16	0.0608	1.10	595	7	602	6	99
Zr41	**4**	**371**	**438**	**1.2**	**126.4**	**1.14**	**0.0512**	**1.76**	**50.8**	**0.6**	**55.2**	**0.97**	**92**
Zr42	50	326	91	0.3	6.576	1.16	0.0696	1.05	913	10	914	7	100
Zr43	**9**	**895**	**787**	**0.9**	**126.4**	**1.14**	**0.0621**	**1.22**	**50.8**	**0.6**	**66.5**	**0.86**	**76**
Zr44	18	435	226	0.5	26.69	1.15	0.0653	1.07	237	3	295	3	80
Zr45	11	161	122	0.8	17.30	1.16	0.0593	1.11	362	4	393	4	92
Zr47	21	348	152	0.4	17.11	1.16	0.0614	1.11	366	4	408	4	90
Zr48	43	342	114	0.3	7.988	1.16	0.0654	1.05	760	8	767	6	99

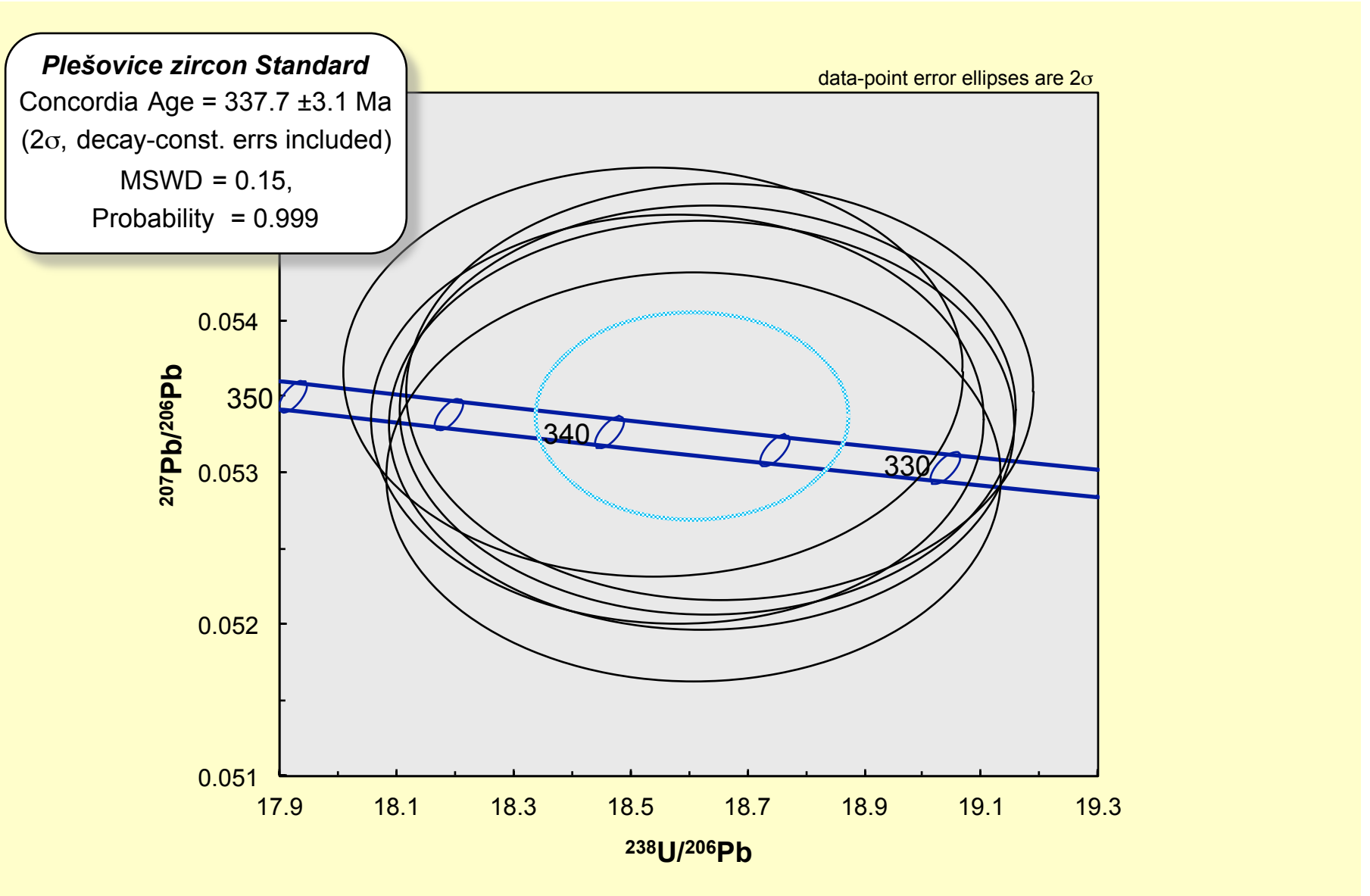
Plešovice zircon Standard
Concordia Age = 337.7 ±3.1 Ma
(2σ, decay-const. errs included)
MSWD = 0.15,
Probability = 0.999
data-point error ellipses are 2σ
0.054
0.053
0.052
0.051
350
340
330
17.9
18.1
18.3
18.5
18.7
18.9
19.1
19.3
207Pb/206Pb
238U/206Pb

	East Xining (m)	Cajiia (m)	Xiejia (m)
Base C22n	101.7	67.35	43.5
Top C22n	123.5	84.5	62.65
Base C21n	159.85	123	98.5
Top C21n	219.1	169	141.9
Base C20n	286.05	259	205.05
Base C18n	352		

Sample	Strat. Pos. (	forced? (	Number of	Declination	Inclination	MAD	Min Temp i	Max Temp	VGP latitud	VGP Longit	Angle from the mean
EX008	4.8	o	4	42.2	53.4	9.4	300	450	55.7	183.5	20.2
EX10	6.6	o	4	239.9	-16.4	5	300	450	-29	23.7	136.7
EX011	7.2	o	4	-21.2	61.3	4.5	300	450	72.7	38.1	31.3
EX11	7.2	o	4	-15.7	64.3	3.1	300	450	74.9	55.7	30.5
EX13	8.5	o	4	42.3	29.3	5.2	300	450	47.2	209.7	22.6
EX013	8.5	o	4	33.1	37.8	5.4	300	450	57.4	210.9	11.7
EX14	12	o	3	192.3	-35.5	2.1	300	400	-69.9	66.1	172.7
EX20	18.6	o	4	211.6	-42.8	7.2	300	450	-60.6	26.3	170.1
EX39	48.1	o	4	254.7	-46.6	4.9	300	450	-27.8	356.4	139.9
EX044	49.6	o	4	236.8	-37.7	1.4	300	390	-38.7	13	150.4
EX46	51	o	4	218.9	-21	0.7	300	450	-46.5	38.1	153.5
EX47	51.2	o	4	229.2	-13.5	8.9	300	450	-36.3	33.1	141.7
EX48	51.4	o	4	233.5	-12.5	2.6	300	450	-32.7	30.2	138.2
EX49	51.6	o	4	238.1	-49.6	1.2	300	450	-41.9	1.5	151.2
EX053	54.2	o	4	254.2	-43.6	6.4	300	450	-27	359	139.5
EX53	54.2	o	4	219.6	-32.6	4.7	300	450	-50.4	29.5	161.2
EX55	56.5	o	4	219	-13.6	3.2	300	450	-43.7	42.1	147.3
EX057	56.9	o	4	241.3	-33.3	4.6	300	450	-33.5	13.3	145.4
EX59	59.1	o	4	243.2	-39.3	1.3	300	450	-34.1	8.1	146.2
EX062	61	o	4	232.2	-32.1	2.2	300	450	-40.4	20.1	151.7
EX63	61.4	o	4	241.8	-16.3	4.9	300	450	-27.5	22.5	135.4
EX068	63.7	o	4	248.3	-32.9	5.7	300	450	-27.8	9.5	140
EX72	65.6	o	4	234.3	-31	2.7	300	450	-38.3	19.4	149.6
EX92	77.6	o	4	224.9	-26.2	2.8	300	450	-44	29.6	153.7
EX93	77.9	o	4	244.8	-19.4	2.6	300	450	-26.1	19	135.2
EX94	78.4	o	4	235.8	-12.7	3.7	300	450	-31	28.4	136.9
EX99	82.7	o	4	234	-10.4	4	300	450	-31.6	30.7	136.3
EX100	83	o	4	222.8	-17.5	2.9	300	450	-42.4	36.4	148.6
EX107	86.4	o	4	252	-44.4	3.4	300	450	-29	359.5	141.2
EX108	87.5	o	4	239.2	-42.3	2.5	300	450	-38.4	7.9	149.9
EX109	89.1	o	4	60.4	39.9	2.9	300	450	36.6	189.1	31.6
EX113	91.5	o	4	61.9	24.5	2.5	300	450	30.1	198.2	39.5
EX115	93.2	o	4	66.3	51.8	3.8	300	450	36.3	175.5	34
EX118	94.4	o	4	74	38.5	5.8	300	450	25.2	182.8	42
EX121	96.4	o	4	242.5	-16.6	5	300	450	-27.1	21.9	135.1
EX123	98.5	o	4	213.8	-24.6	2.3	300	450	-51.5	41.1	159.2
EX127	101.4	o	4	255.6	-37	1.8	300	450	-23.4	2.9	136.3
EX128	102	o	4	54.2	40	3.2	300	450	41.6	192.7	27
EX130	103.6	o	4	50	35.6	1.5	300	450	43.4	199.1	25.2
EX137	108	o	4	38	32.8	13.1	300	450	51.7	210.7	17.6
EX138	112.2	o	4	222.1	-62.6	5.2	300	450	-57.4	345.4	154.2
EX139	113.4	o	4	23	26.4	2.2	300	450	59.4	233.6	15.1
EX141	114.8	o	4	59.1	35.9	2.5	300	450	36.2	192.9	31.9
EX145	117.5	o	4	31.9	23.8	5.8	300	450	52.6	223.8	20.5
EX147	119	o	4	31.1	78.6	3	300	450	54	121	38
EX149	120.4	o	4	29.9	60.6	5.8	300	450	66.4	170.5	20.8
EX150	121.6	o	4	56	64.7	5.4	300	450	47.8	160	31.9
EX155	125.4	o	4	244.5	-23.9	1.8	300	450	-27.8	16.9	138.2
EX169	135	o	4	201.8	-36.1	0.7	300	450	-64.7	47	174.4
EX172	137.1	o	4	220.4	-54.2	1.6	300	450	-57.3	2.9	160.3
EX175	139.9	o	4	216	-31	2.1	300	450	-52.5	34.2	162.7
EX177	141.6	o	4	213.5	-19.8	3.5	300	450	-49.9	44.4	155.3
EX178	142.2	o	4	235.8	-20.8	6	300	450	-33.7	24.4	142.6
EX185	148.4	o	4	237	-31.6	2.1	300	450	-36.4	17.2	147.8
EX187	150.3	o	4	233.7	-42	1.3	300	450	-42.7	11.2	153.8
EX196	156.2	o	4	226.4	-24.2	1	300	450	-42.1	29.5	151.3
EX199	157.9	o	4	224	-25	6.9	300	450	-44.3	31.1	153.4
EX201	158.6	o	4	227.7	-37.4	6.3	300	450	-45.9	19.1	157.2
EX203	159.3	o	4	225.7	-25.8	6.4	300	450	-43.2	29.1	152.8
EX205	159.4	o	4	222.3	-22.5	3.1	300	450	-44.6	34.1	152.8
EX207	160.3	o	4	-41.2	60.5	8.6	300	450	57.9	33.6	40.7
EX209	161.4	o	4	-31.7	65.9	6.7	300	450	64.1	48.6	37.2
EX211	162.8	o	4	62.6	34.3	2.1	300	450	32.8	NaN	35.2
EX215	167.1	o	4	35.2	23.2	2.9	300	450	50	220.5	22.7
EX219	169.3	o	4	46.5	39.9	2.5	300	450	47.7	197.8	21.2
EX223	171	o	4	51.4	33.3	3	300	450	41.5	199.8	27.1
EX227	174	o	4	50.5	42.2	2.2	300	450	45.4	193	23.8
EX229	174.8	o	4	65.6	50	1	300	450	36.2	177.6	33.6
EX231	179	o	4	53.1	42.1	2.3	300	450	43.2	191.5	25.7
EX235	181.6	o	4	50.3	37.3	4.4	300	450	43.8	197.4	24.8
EX237	185	o	4	55.7	29.9	3.2	300	450	36.9	199.2	32
EX238	185.3	o	4	54.4	16.2	1.9	300	450	33.3	207.7	39.6
EX239	186.7	o	4	47.2	32	0.6	300	450	44.3	203.7	24.6
EX241	187.4	o	4	16	22.5	1	300	450	61.2	247.7	18.6
EX243	190.7	o	4	57.6	40.2	2.2	300	450	38.9	190.6	29.4
EX245	191.4	o	4	53.2	20.9	2.2	300	450	35.7	206.2	35.6
EX248	192.7	o	4	40	8.3	1.3	300	450	41	223.6	37.9
EX249	194.3	o	4	41.2	25.2	1.8	300	450	46.4	213.4	24.6
EX250	194.6	o	4	79.5	41.3	1.7	300	450	22	178	44.9

EX251	200.1 o	4	68.5	47	2.2	300	450	32.8	179	35.8
EX252	200.8 o	4	66.6	38.3	1.5	300	450	31	186.9	36.7
EX253	201.2 o	4	39.8	72.1	6.9	300	450	56.6	141	32.8
EX254	209.6 o	4	76.6	55.5	2.2	300	450	30.1	167.2	39.9
EX255	210 o	4	228.2	-32	2.9	300	450	-43.5	23	154.6
EX256	210.5 o	4	33.5	22.1	1.1	300	450	50.8	223	22.7
EX257	212.3 o	4	59.3	19.1	2.3	300	450	30.4	202.8	41
EX258	212.5 o	4	52.3	25.7	1.1	300	450	38.1	204.1	31.8
EX259	212.9 o	4	31.3	66.3	1.6	300	450	64.2	153.9	26.3
EX260	213.1 o	4	42.1	59.1	4.2	300	450	57.1	173	23.4
EX261	213.4 o	4	52.3	51.8	2.5	300	450	47.3	181.5	25.4
EX262	215 o	4	64.1	27	1.4	300	450	29.2	195.5	39.8
EX263	215.6 o	4	224.1	-10.7	2.9	300	450	-39	38.7	142.2
EX266	217.9 o	4	46.2	43.7	6.1	300	450	49.4	194.2	20.5
EX271	223.2 o	4	216.6	-5.3	3.1	300	450	-42.2	48.4	140.8
EX272	225.9 o	4	243.6	-35.5	2.4	300	450	-32.4	10.5	144.5
EX275	232.3 o	4	231.9	-13.2	2.7	300	450	-34.2	31	139.8
EX274	232.4 o	4	232	-52	4.5	300	450	-47.5	1.3	154.7
EX281	241.6 o	4	243.4	-22.5	7.4	300	450	-28.3	18.3	138.2
EX283	241.8 o	4	238.1	-26.9	3.3	300	450	-33.9	19.4	144.6
EX285	242 o	4	227.2	-16.8	1.7	300	450	-38.9	33	145.5
EX289	248.3 o	4	231.1	-18.6	5.9	300	450	-36.6	28.9	144.3
EX293	253.5 o	4	45.6	27.4	1.5	300	450	43.9	208.2	26
EX294	253.8 o	4	61.4	41.6	3.3	300	450	36.4	187.3	31.9
EX296	258 o	4	47	25.4	10.3	300	450	42.1	208.3	28.3
EX300	278.1 o	4	229	-52.4	1.2	300	450	-50	2.1	156.4
EX301	278.4 o	4	240.8	-34.7	2.4	300	450	-34.4	12.7	146.4
EX303	279.6 o	4	219.7	-22.6	0.7	300	450	-46.6	36.4	154.4
EX311	283.8 o	4	251.8	-35.6	2	300	450	-25.9	5.9	138.5
EX312	284 o	4	247.5	-30.3	3.9	300	450	-27.5	11.5	139.3
EX314	288.1 o	4	64.4	40.3	1.5	300	450	33.5	186.6	34.4
EX317	291.8 o	4	73.3	68.5	2.1	300	450	37.7	150.3	39.7
EX319	292.6 o	4	34.5	22.2	5.9	300	450	50.2	221.9	23.1
EX321	292.8 o	4	19	72.2	3.5	300	450	65.8	127.4	31.2
EX323	294.8 o	4	50.9	30.2	1.4	300	450	40.8	202.3	28.2
EX325	295.8 o	4	50	47.7	2.1	300	450	47.7	187.5	23.3
EX327	297 o	4	50.9	27.4	2.2	300	450	39.8	204.1	29.8
EX329	297.5 o	4	47.2	61.4	1.7	300	450	53.6	167.6	26.8
NX1.1	298 o	4	62.7	26.3	2.8	300	450	30	196.7	39.2
NX4.2	334 o	4	236.7	-30.8	2.7	300	450	-36.3	17.9	147.7
NX6.1	346 o	4	196.8	-27.5	0.5	300	450	-63.4	63.2	166.5
NX7.2	358 o	4	46.9	44.6	2.9	300	450	49.1	192.8	21
NX9.1	370 o	4	-18.6	66.2	4.3	300	450	71.9	59.1	32.5
NX10.1	371 o	4	15	39.8	2.2	300	450	71	234.9	2.9
NX11.2	375.5 o	4	26.9	45.5	3.7	300	450	65.3	207.1	7.6
NX12.1	378 o	4	33.3	37.8	4.9	300	450	57.3	210.7	11.8
45 cutoff										
EX1	0.6 o	4	230.8	7	3.3	300	450	-28.1	40.7	123.6
EX3	2.2 o	4	-86.6	12.8	6.7	300	450	6.6	15.1	92.7
EX7	4.4 o	4	-80.4	3.1	6.7	300	450	8.6	7.4	94.7
EX9	5.4 o	4	248.4	4.5	6.6	300	450	-15.8	27	115.6
EX15	13.7 o	4	-75.7	-13	7.8	300	450	7.4	358	101.6
EX16	14.2 o	4	267.8	30.8	6.4	300	450	8.1	26.6	83.9
EX17	15.3 o	4	256.9	-1.9	7.5	300	450	-11.1	19	114.6
EX18	17 o	4	267.8	28.3	3.4	300	450	7.2	25.4	85.6
EX19	18.3 o	4	216.8	5.4	9.2	300	450	-37.9	52.6	130.7
EX35	47 o	4	237.4	-5.5	1.2	300	450	-27.4	30.4	130.4
EX37	47.6 o	4	236.5	-6.1	9.9	300	450	-28.3	30.8	131.4
EX43	49.4 o	4	241	-14.3	1.8	300	450	-27.5	24	134.5
EX51	52.5 o	4	242.5	-2.2	3	300	450	-22.5	28.3	124.6
EX52	53 o	4	-88.4	-18.9	3.9	300	450	-4.5	3.1	114.8
EX67	62.9 o	4	236.6	-0.4	3.6	300	450	-26.4	33.2	126.8
EX71	65 o	4	253.6	8.3	2.3	300	450	-10.6	25.2	109.4
EX072	65.6 o	4	264.2	-28.5	3.8	300	450	-13.5	2.9	125.8
EX094	78.4 o	4	-81.8	-42.7	2.8	300	450	-8.4	347.2	123
EX95	79.2 o	4	259.1	-4.9	5.9	300	450	-10.2	16.4	115.2
EX97	81.7 o	4	253	-25.5	3.1	300	450	-21.5	10.9	132.7
EX98	82.6 o	4	244.4	-17.4	4.6	300	450	-25.8	20.2	134.2
EX099	82.7 o	6	229.8	-1.2	11	300	450	-31.6	38.1	131.1
EX101	83.4 o	4	260.1	-10.7	4.3	300	450	-11.2	13.5	118.4
EX102	83.8 o	4	254.9	-2.4	2.1	300	450	-12.8	20.1	116.4
EX103	84.2 o	4	251.6	-18.9	4	300	450	-20.6	15	129.9
EX104	84.8 o	4	-75.9	-64.5	5.9	300	450	-17.2	326.5	128.1
EX105	85 o	4	-78.6	13.5	2.5	300	450	13.2	10.6	86.5
EX106	85.6 o	4	239.5	-8.3	3.8	300	450	-26.7	27.7	131.1
EX110	89.6 o	4	54.5	-3.3	1.7	300	450	26.7	216.3	55.1
EX111	90.1 o	4	83.5	33.5	1.9	300	450	15.9	180.6	51.1
EX112	90.8 o	4	75.2	19.8	0.9	300	450	17.9	192.3	52.3
EX114	92.2 o	4	92.7	58.8	3.8	300	450	20.5	157.2	48.1
EX116	93.6 o	4	76.6	23.4	7.7	300	450	18	189.8	51.2

EX117	93.8 o	4	80.9	30.7	7.8	300	450	16.9	183.6	50.6
EX119	94.6 o	4	-87	0.7	10.3	300	450	2.6	10.4	101.2
EX120	95.6 o	4	246.4	-9.9	6	300	450	-21.8	22.3	127.7
EX122	98 o	4	257.4	17.3	2.6	300	450	-4.7	26.6	100.3
EX124	99.4 o	4	254.1	-25.4	6.4	300	450	-20.6	10.3	131.8
EX125	99.7 o	4	249.5	-0.5	4.7	300	450	-16.5	24.2	118.8
EX131	104.6 o	4	92.3	42.9	2.1	300	450	12.8	170.2	53.1
EX133	105.9 o	4	63.2	13.2	2.6	300	450	25.4	203	47.7
EX151	122.6 o	4	156.6	-11	8.7	300	450	-52.3	142.2	132.6
EX153	124 o	4	250.2	-13.8	1.8	300	450	-20.1	18.2	127.7
EX157	127 o	4	266.3	-36.4	1.8	300	450	-14.7	357.4	128.2
EX165	132.9 o	4	234.9	-8.1	4.4	300	450	-30.2	31.1	133.9
EX173	139 o	4	236.1	-3.3	4.6	300	450	-27.7	32.3	129.4
EX181	144.5 o	4	246.9	-11.9	10.4	300	450	-22.1	21.1	128.7
EX183	145.7 o	4	251.1	-8	3.3	300	450	-17.6	20.1	123.1
EX189	151.4 o	4	241.5	-6.9	3.1	300	450	-24.7	26.9	128.8
EX191	152.6 o	4	238.8	-2.8	8.2	300	450	-25.5	30.6	127.4
EX193	154.2 o	4	250.5	-6.2	5	300	450	-17.5	21.3	122.2
EX195	155.6 o	4	-84.8	-3	3.9	300	450	3.3	7.6	102
EX197	156.8 o	4	264.5	-16.9	3.3	300	450	-9.5	8.2	119
EX247	192.1 o	4	97.2	27.2	3	300	450	2.9	176.1	64.5
EX264	215.8 o	4	90.4	71.1	4	300	450	29.2	142.3	45.8
EX265	216.7 o	4	-36.6	-52.8	2.8	300	450	12.2	312.5	105.1
EX267	220.3 o	4	266.3	-10.1	4.7	300	450	-6	10	113.3
EX268	220.6 o	4	256.1	-31.5	5.4	300	450	-21.1	5.8	133.5
EX270	223.1 o	4	246.8	1.6	9.6	300	450	-18	26.9	119
EX276	233.5 o	4	266.2	-32.5	3.6	300	450	-13.4	359.7	126.4
EX280	240.3 o	4	100.1	51.4	7.6	300	450	11.4	160.2	54.4
EX287	245 o	4	254.6	6.8	4.4	300	450	-10.3	24	109.9
EX288	245.5 o	4	-89.7	-6.7	10.3	300	450	-1.8	9	108.1
EX291	248.8 o	4	264.6	-5.7	7.5	300	450	-6	12.8	111.7
EX307	281.6 o	5	-88.8	-29.1	7.4	300	450	-8.2	358.6	121
EX309	282.9 o	4	251.8	-27.6	2.1	300	450	-23.2	10.5	134.7
EX313	285.4 o	5	258.8	-4.1	4.1	300	450	-10.2	17	114.8
EX315	291 o	4	82	31.1	2	300	450	16.2	182.7	51.2
EX331	297.7 o	4	79.2	11.6	6	300	450	12.2	193.6	60.4
NX5.2	338.5 o	4	-89.7	-58.6	3.3	300	450	-22	338.5	133.1

Sample	Strat. Pos. (	forced? (o=	Number of	Declination	Inclination	MAD	Min Temp i	Max Temp	VGP latitud	VGP Longit	Angle from the mean
15XCJ038A	10.25	o	7	183.3	-8	1.2	320	620	-57.3	95.8	145.9
15XCJ039A	10.5	o	8	187.5	-30.4	1	320	670	-68.7	81.8	164.2
15XCJ040A	10.9	o	9	241.3	-41.3	1.5	320	670	-36.4	7.6	151.5
15XCJ041A	11.4	o	8	205.8	-7.1	1.1	320	670	-49.3	60.2	151.6
15XCJ042A	11.75	o	8	202.1	-14.8	1.6	320	670	-54.6	61.9	159.1
15XCJ043A	12	o	9	206.9	-23.6	1.8	320	670	-55.7	50.2	168
15XCJ044A	12.4	o	8	214	-43.3	1.6	320	670	-58.9	23.8	169.8
15XCJ045A	13.1	o	8	190	-28.6	1	320	670	-66.9	76.6	165.3
15XCJ046A	13.5	o	8	227.8	-44.3	1.2	320	630	-48.3	12.7	160.8
15XCJ047A	14	o	7	190.7	-55.9	1.6	320	620	-81.4	9.5	157.2
15XCJ048A	14.6	o	8	214.9	-21.3	1.7	320	670	-49.5	42.2	163.5
15XCJ049A	14.9	o	9	189.2	-59.4	1.9	320	670	-81.9	342.9	153.9
15XCJ050A	15.25	o	8	195.5	-23.7	1.2	320	670	-62	68.1	165.4
15XCJ051A	16	o	8	199.8	-38.3	1.3	320	670	-67.1	47.7	174.7
15XCJ052A	16.5	o	9	196.8	-44.7	2.7	320	670	-72.4	43.1	168.7
15XCJ053A	17	o	8	185.7	-50.3	1.2	320	670	-82.8	60	159.4
15XCJ054A	17.5	o	8	215.2	-37	1.1	320	670	-55.5	29.8	172
15XCJ055A	18	o	9	206.6	-8.2	1	320	670	-49.4	58.8	152.6
15XCJ056A	18.5	o	8	205.4	-46.4	1.3	320	670	-66.9	27.2	169.1
15XCJ057A	19	o	8	232.6	-24.6	1.9	320	670	-37.5	24.7	154.2
15XCJ001A	19.5	o	8	176.9	-22.9	3.2	320	630	-65.2	109.3	152.3
15XCJ058A	19.6	o	8	214.5	-33.8	0.8	320	630	-54.8	33.5	172.4
15XCJ002A	20	o	7	161.9	-69.2	3.4	320	620	-69.5	249.5	138.8
15XCJ059A	20	o	8	192	-35.8	2.4	320	670	-70.2	66.8	169.1
15XCJ003A	20.5	o	8	238.4	-17.5	2.8	320	670	-30.5	24.3	145.7
15XCJ060A	20.5	o	8	219.6	-40.4	1.7	320	670	-53.4	22.5	167.8
15XCJ004A	21	o	8	199.4	-34.2	0.9	320	630	-65.3	53	174.9
15XCJ061A	21	o	8	197.4	-75	3.1	320	630	-62.6	300	140.4
15XCJ005A	21.5	o	7	185.3	-12	2.7	320	620	-59.1	91.7	150.3
15XCJ006A	22	o	7	237.6	-24.6	5.4	320	620	-33.5	21.2	150.3
15XCJ007A	22.5	o	8	218.8	-23	1.5	320	630	-47.4	37.1	162.9
15XCJ008A	23	o	7	175.8	-10.3	1	320	620	-58.4	110	143.2
15XCJ009A	23.5	o	8	194.5	-28	1.3	320	670	-64.7	67.5	168.1
15XCJ010A	24	o	8	186.8	-27.4	0.6	320	630	-67.1	84.9	162.2
15XCJ011A	24.5	o	7	176.2	-16.4	2.2	320	620	-61.6	110	147.7
15XCJ012A	25	o	7	187	-29.2	1.9	320	620	-68.1	83.6	163.3
15XCJ013A	25.5	o	7	192.3	-35.2	0.9	320	630	-69.7	66.6	169.3
15XCJ014A	26	o	7	195.8	-18.2	0.7	320	620	-59.2	70.4	160.7
15XCJ015A	26.5	o	7	195.9	-18.2	1.4	320	670	-59.1	70.1	160.7
15XCJ016A	27	o	8	194.7	-27.1	1.4	320	630	-64.2	67.5	167.7
15XCJ017A	27.5	o	7	210.6	-24.5	0.9	320	620	-53.8	45	168.1
15XCJ019A	28.5	o	8	222	-41.8	3.1	320	630	-52	19.2	165.6
15XCJ020A	29	o	7	162.7	-17.2	1.8	320	620	-58.1	135.7	138
15XCJ021A	29.5	o	8	191.6	-60.7	1.8	320	670	-79.7	338.8	153.3
15XCJ022A	30	o	8	32.1	-2.5	1.7	320	630	41.8	236.5	38.5
15XCJ023A	30.5	o	8	201.6	-29.2	3.2	320	670	-61.6	53.9	172.9
15XCJ024A	31	o	7	261.4	-58.2	3.8	320	620	-27.9	342.5	137.2
15XCJ025A	31.5	o	8	205.8	-37.5	1.8	320	630	-62.7	39.7	178
15XCJ026A	32	o	7	204	-25.4	1.1	320	620	-58.3	53	169.8
15XCJ027A	32.5	o	8	209.5	-38	2.2	320	670	-60.2	34.6	175.9
15XCJ028A	33	o	8	212.5	-23.2	2.7	320	630	-51.9	43.7	166.2
15XCJ029A	33.5	o	7	4.5	7	2.8	320	620	56.6	273.9	34.4
15XCJ062A	33.75	o	8	168	-19.7	1.5	320	670	-61.4	127.3	143.5
15XCJ030A	34	o	7	208.8	-44.2	3.6	320	670	-63.3	27.4	171
15XCJ072A	41.6	o	8	3.7	45.9	3.4	320	630	80.1	262.3	19.3
15XCJ074A	42	o	8	224.3	-25.2	1.7	320	670	-44.1	30.8	160.8
15XCJ075A	42.3	o	8	227.2	0.2	1.9	320	670	-33	40.9	138.9
15XCJ076A	42.75	o	3	205.3	-12.6	7.8	540	630	-52	58.4	157.1
15XCJ077A	43.75	o	7	197	-49.1	1.4	320	670	-74.3	32.1	165.1
15XCJ078A	44	o	8	211.3	-37.2	2.5	320	630	-58.6	33.6	175
15XCJ080A	44.75	o	7	215.2	-5.3	1.3	320	620	-43.1	49.9	148.5
15XCJ081A	45.5	o	7	203.7	-35.2	2.2	320	620	-63.1	45.2	178.5
15XCJ082A	46	o	8	208.7	-19.8	4.2	320	630	-53	50.3	164.1
15XCJ083A	46.5	o	8	213	-43.8	2.3	320	670	-59.9	23.8	169.8
15XCJ084A	47	o	7	223.1	-15.9	1.4	320	620	-41.7	37.2	154.8
15XCJ085A	47.5	o	8	228.4	-38.2	1.5	320	630	-45.6	18.1	161.5
15XCJ086A	48	o	7	215	-40.1	2	320	620	-56.9	26.7	171.2
15XCJ087A	48.5	o	8	185.2	-2.8	1.1	320	670	-54.5	93.1	142.3
15XCJ088A	48.9	o	9	162.1	-20	1.3	320	670	-59.2	138	139.1
15XCJ090A	49.8	o	7	207.2	-25	1.7	320	620	-56.2	48.9	169.4
15XCJ091A	50.5	o	8	181.1	-48.3	2.4	320	630	-82.7	94.7	158
15XCJ092A	51	o	7	206.5	-49.5	3.4	320	620	-67.1	20.1	166
15XCJ093A	51.5	o	8	220.8	-34.1	1.2	320	670	-50.1	27.3	167.3
15XCJ094A	52	o	8	209	-36.6	0.9	320	630	-60	36.8	176.9
15XCJ095A	52.2	o	7	197.9	-30.4	2.1	320	620	-64.2	59.2	171.9
15XCJ096A	52.5	o	7	200.9	-40.4	1.7	320	620	-67.5	43.2	174
15XCJ097A	53	o	4	221.9	-28	1.3	490	630	-46.9	31.1	164.1
15XCJ098A	53.5	o	8	191.6	-32.2	3.2	320	670	-68.3	70.6	168.1
15XCJ099A	54	o	7	194.8	-40.4	1.3	320	620	-71.4	54.4	170.3

15XCJ100A	54.5 o	8	202.8	-44.7	2.2	320	630	-68.1	33.5	170.5
15XCJ101A	55 o	7	197.8	-49.8	1.8	320	620	-74	28.8	164.7
15XCJ102A	55.5 o	7	4.5	32.4	2.2	320	620	70.6	269	17.6
15XCJ103A	56.1 o	8	35.8	47.2	4.2	320	630	58.9	196.8	14.1
15XCJ104A	56.5 o	7	40.9	43.4	2.3	320	620	53.5	198.1	14.3
15XCJ105A	57 o	8	9	40.5	1.1	320	670	74.5	249.6	13.9
15XCJ106A	57.3 o	8	20.9	38.2	1.6	320	630	66.4	226.2	4.5
15XCJ107A	57.9 o	7	19.7	42.7	2.2	320	620	69.4	221.5	8.5
15XCJ108A	58.5 o	7	17.4	53.1	2	320	620	75.4	198.7	18.4
15XCJ109A	58.9 o	8	12.7	25.7	2.6	320	630	64.3	252.5	14.7
15XCJ110A	59.5 o	7	31.4	26.5	5.9	320	620	54	222.7	10.4
15XCJ112A	60.25 o	9	178.2	-31	2.5	320	670	-70.1	106.9	156.9
15XCJ113A	61 o	7	226	-32.7	4.4	320	620	-45.5	24.3	162.7
15XCJ114A	61.5 o	8	227.1	-53.9	2.2	320	670	-52	0.8	156.2
15XCJ115A	62 o	8	234.4	-69.4	2	320	630	-49.3	330.3	142.5
15XCJ116A	62.3 o	8	184.2	-35.9	2.5	320	670	-72.9	88.3	162.8
15XCJ117A	63 o	8	201	-21.8	2.1	320	670	-58.4	59.9	165.8
15XCJ118A	63.5 o	3	246	-48.9	10.1	540	630	-35.5	358.7	147.6
15XCJ119A	64 o	7	175.9	-46.8	2.6	320	620	-80.8	125.3	155.3
15XCJ120A	64.5 o	8	202.4	-15.5	1.8	320	670	-54.8	61.1	159.9
15XCJ121A	65 o	9	175	-36.9	2.6	320	630	-73.4	118.4	155.6
15XCJ122A	65.7 o	8	195.1	-25.6	1.8	320	670	-63.2	67.8	166.7
15XCJ123A	66 o	8	173.8	-44	2.1	320	670	-77.9	129.5	154.5
15XCJ124A	66.5 o	4	212.2	-27	11.1	490	630	-53.6	41.4	169.7
15XCJ125A	67 o	8	196	-28.4	2.1	320	670	-64.2	64.2	169.4
15XCJ126A	67.7 o	7	-18.9	17.5	8.5	320	620	57.5	318.4	43.1
15XCJ127A	68 o	8	38.3	40.7	3.9	320	630	54.5	203.2	11.4
15XCJ128A	68.5 o	6	7.1	36.8	1.6	370	620	72.7	258.9	14.8
15XCJ129A	69 o	8	41.9	26.2	3.4	320	670	46.3	212.2	16.9
15XCJ130A	69.5 o	8	25.2	26.4	1.8	320	630	58.1	230.7	9.1
15XCJ131A	70 o	7	42.8	68.6	5.6	320	620	56.4	151.3	34.5
15XCJ132A	70.5 o	7	15.2	30.5	3.6	320	620	65.7	244.3	9.9
15XCJ133A	71 o	8	6.9	33.9	1.4	320	630	71	261.4	15.2
15XCJ134A	71.5 o	7	30.2	22.9	2.5	320	620	53.3	226.4	13.3
15XCJ135A	72 o	8	43.1	12.9	3.4	320	670	40.5	218.7	27.7
15XCJ137A	73 o	7	-4.4	11.7	2.2	320	620	59	290.6	36
15XCJ138A	73.5 o	7	30	23.5	2.5	320	620	53.7	226.4	12.6
15XCJ139A	74 o	8	53.4	18.9	3.2	320	630	34.9	207.2	29.7
15XCJ142A	75.5 o	9	15.9	20.5	4.1	320	670	60.3	249.1	17.2
15XCJ147A	78 o	7	7	22.3	7.1	320	620	64.2	266	20.7
15XCJ148A	78.5 o	8	17.3	10.6	3.8	320	670	55	250.9	25.9
15XCJ149A	79 o	8	-4.9	17.7	3.1	320	630	62.1	292.4	32.2
15XCJ151A	80 o	7	-10.4	36.1	3.7	320	620	71.1	313.6	28.9
15XCJ152A	80.5 o	7	3.2	30.5	3.7	320	620	69.6	273	19.2
15XCJ153A	81 o	9	-0.8	56.6	4	320	670	89.1	53	27.5
15XCJ154A	81.5 o	8	25.9	48	2.3	320	670	67.1	203.8	12.5
15XCJ157A	82.45 o	8	54.3	22.4	5	320	670	35.4	204.6	28.3
15XCJ156A	82.55 o	9	10.3	15.3	1.4	320	670	59.7	261.5	24.3
15XCJ158A	83 o	8	-28.8	43.3	3.1	320	670	63	355.3	41.8
15XCJ159A	83.5 o	8	-14.1	61.5	3.7	320	630	77.6	45.4	35.9
15XCJ160A	83.95 o	8	4.9	49.7	2.3	320	670	82.7	247.1	20.6
15XCJ162A	85.05 o	9	194.4	-29.9	3.5	320	670	-65.7	66.3	169.2
15XCJ163A	85.5 o	8	233.7	-22.9	2.7	320	670	-36.1	24.8	152.4
15XCJ164A	86 o	3	220.7	-55.3	6.6	570	670	-57.4	0.8	157.6
15XCJ165A	86.5 o	9	244.8	-39.7	2.5	320	670	-33	7	148.8
15XCJ166A	87 o	8	210.5	-42.4	3.1	320	670	-61.3	28.2	172.1
15XCJ167A	87.5 o	8	229.7	-40.6	2.4	320	670	-45.4	15.1	160.3
15XCJ168A	87.98 o	9	211.5	-45.5	4.3	320	670	-61.7	22.8	169
15XCJ169A	88.45 o	8	229.7	-28.7	5.8	320	670	-41.2	24.2	158.4
15XCJ170A	89 o	8	199.1	-23.5	1.9	320	670	-60.2	61.9	166.8
15XCJ171A	89.4 o	9	218.5	-26.2	3.3	320	670	-48.8	35.4	165.5
15XCJ172A	90.02 o	8	211.2	-37.4	1.9	320	670	-58.7	33.4	175
15XCJ173A	90.45 o	8	239.7	-47	2.9	320	670	-39.7	3.5	152.1
15XCJ174A	90.97 o	9	189.5	-48.5	2	320	670	-79.3	51.2	162.5
15XCJ175A	91.5 o	8	193.7	-46.1	1.5	320	670	-75.2	46.7	166.2
15XCJ176A	92 o	8	199.1	-40.5	1.3	320	670	-68.7	46	172.9
15XCJ177A	92.4 o	9	197.2	-34.8	2.2	320	670	-67	56.6	173.2
15XCJ178A	93 o	8	241.8	-44.8	3.4	320	670	-37.2	4.4	150.9
15XCJ179A	93.45 o	8	229.3	-21.6	1.4	320	670	-39	28.9	154.9
15XCJ180A	94.03 o	9	219.1	-25.2	1.3	320	670	-47.9	35.4	164.3
15XCJ181A	94.5 o	8	214.3	-38.4	1.2	320	670	-56.7	29.2	172.3
15XCJ182A	95 o	8	209.8	-30.2	1.5	320	670	-56.7	41.7	173.5
15XCJ183A	95.5 o	9	228.5	-46	1.9	320	670	-48.3	10.4	159.7
15XCJ184A	96 o	8	187.8	-35.8	2.7	320	670	-71.9	77.7	165.7
15XCJ185A	96.5 o	8	211	-47.6	1.5	320	670	-62.9	20	167.2
15XCJ186A	97 o	8	210.4	-40.7	1	320	670	-60.6	30.5	173.5
15XCJ187A	97.5 o	8	190.3	-24.6	1.8	320	670	-64.5	78.2	163
15XCJ189A	98.5 o	7	177.1	-31.2	0.9	320	630	-70	110.1	156.1
15XCJ190A	99 o	7	215.4	-63.5	1.5	320	620	-62.2	343.2	151.3
15XCJ191A	99.5 o	7	227.1	-31.9	3	320	620	-44.4	24	161.7

15XCJ192A	100 o	8	217.1	-34.9	2.5	320	630	-53.2	29.9	170.4
15XCJ194A	101 o	8	222.7	-12.1	1.1	320	670	-40.6	39.4	151.9
15XCJ195A	101.5 o	8	216.8	-26.7	1.5	320	630	-50.3	36.7	166.9
15XCJ196A	102 o	8	214.4	-17.8	3.6	320	670	-48.5	44.7	160.6
15XCJ197A	102.5 o	8	227.6	-9.6	1.7	320	670	-36.2	36.3	147.2
15XCJ198A	103 o	9	208.9	-21.8	1.3	320	670	-53.7	48.8	166
15XCJ199A	103.5 o	8	189.2	-22.5	1.9	320	670	-63.7	81.3	160.8
15XCJ200A	104 o	8	202.5	-45.3	3.2	320	670	-68.6	32.8	169.9
15XCJ201A	104.5 o	4	230.8	-47.5	5.3	540	670	-47	7.5	157.7
15XCJ202A	105 o	8	206.6	-21.1	3.6	320	670	-54.9	52.2	165.6
15XCJ203A	105.5 o	4	148.2	-41.8	7.7	470	620	-60	176.4	135.7
15XCJ204A	106 o	9	219.9	-30	5.8	320	670	-49.2	31.4	166.7
15XCJ205A	106.5 o	7	201.3	-22.1	5	320	670	-58.4	59.2	166.1
15XCJ206A	107 o	8	179.3	-10	3.9	320	670	-58.4	103.3	145.2
15XCJ207A	107.5 o	9	192.3	-20	4.2	320	670	-61.5	76	160.7
15XCJ208A	108 o	8	175.2	-34.3	2.8	320	670	-71.7	116.6	155.3
15XCJ209A	108.5 o	8	213.6	-40.3	4.1	320	670	-58	27.7	171.9
15XCJ210A	109 o	9	231.8	-33.7	4.4	320	670	-41.3	19.4	158.3
15XCJ211A	109.5 o	8	184.7	-38.6	3	320	670	-74.6	85.2	163.3
15XCJ213A	110.5 o	8	246.7	-25.4	1.6	320	670	-26.5	14.8	143.3
15XCJ214A	111 o	8	148.5	-46.2	5	320	670	-62	182.2	136.6
15XCJ215A	111.5 o	8	234	-47.7	3	320	670	-44.5	5.6	155.6
15XCJ216A	112 o	9	235.8	-34.1	5	320	670	-38.2	16.4	155.1
15XCJ217A	112.5 o	8	213.6	-36.6	6.3	320	670	-56.6	31.8	173.3
15XCJ218A	113 o	8	218	-25.9	2.1	320	670	-49.1	36.1	165.6
15XCJ219A	113.4 o	9	182	-31.7	2.8	320	670	-70.5	96.3	160.2
15XCJ220A	114 o	8	196.1	-38.1	1.9	320	670	-69.3	55.1	172.1
15XCJ221A	114.5 o	8	211.5	-6	8	320	670	-45.6	53.8	149.9
15XCJ222A	115 o	9	203.5	-43.1	4.1	320	670	-66.8	35.2	172.3
15XCJ223A	115.5 o	8	231.5	-41.6	7.4	320	670	-44.3	13.1	158.8
15XCJ225A	115.9 o	9	209.8	-45.6	7.1	320	670	-63.1	24.2	169.4
15XCJ226A	116.5 o	8	206.9	-61.6	5.4	320	670	-68.6	347.1	153.9
15XCJ227A	117 o	8	205.8	-25.2	3.5	320	670	-57.1	50.7	169.7
15XCJ228A	117.5 o	9	198.2	-22.7	5.3	320	670	-60.3	63.9	165.7
15XCJ229A	118 o	8	204.8	-32.2	2.2	320	670	-61	46.5	176.7
15XCJ230A	118.5 o	8	207.3	-42.8	4.8	320	670	-63.9	31	172.6
15XCJ231A	119 o	9	218.4	-46	5.5	320	670	-56.4	16.7	165.6
15XCJ232A	119.5 o	8	182.8	-37.9	4.3	320	670	-74.4	92.1	161.8
15XCJ233A	120 o	9	226.4	-19.5	7.1	320	670	-40.5	32.4	155.5
15XCJ234A	120.5 o	8	200.6	-26.5	9.4	320	670	-60.9	57.5	170.1
15XCJ235A	121 o	3	214.2	-34.4	6.1	570	670	-55.2	33.2	172.7
15XCJ236A	121.5 o	8	227	-13.3	4.6	320	670	-37.8	35.1	150.4
15XCJ242A	124.5 o	7	14.1	42.8	2.1	320	620	73.2	232.3	11.4
15XCJ243A	125 o	8	44.9	58	1.8	320	630	54.8	174.7	25.9
15XCJ244A	125.5 o	7	74.7	71.4	5.7	320	620	37.8	145.1	43.9
15XCJ245A	125.9 o	7	-8.6	21	5	320	620	63.1	300.8	33
15XCJ246A	126.5 o	8	-10.6	33.5	2	320	630	69.5	311.8	29.5
15XCJ247A	127 o	8	20.3	23.3	1	320	670	59.5	240.1	13
15XCJ248A	127.6 o	8	16	17.3	1.7	320	630	58.6	250.3	20
15XCJ249A	128 o	7	20	39.8	2.8	320	620	67.8	225.3	6.1
15XCJ250A	128.5 o	7	36.3	36.8	2.1	320	620	54.6	208.9	8.9
15XCJ251A	129 o	7	24.5	38.6	2.2	320	620	64.1	220.2	3.2
15XCJ252A	129.5 o	7	25.8	41.4	2.4	320	630	64.4	214.9	5.9
15XCJ253A	130 o	7	16.9	40.5	1.3	320	620	70.2	230.2	8.4
15XCJ254A	130.5 o	7	43.6	65.2	3.1	320	620	56.4	159.7	31.6
15XCJ255A	131 o	8	24.7	35.2	1.9	320	630	62.4	223.7	0.6
15XCJ256A	131.5 o	7	25.9	28.3	4	320	620	58.5	228.3	7.2
15XCJ257A	132 o	7	9.5	38.8	2.9	320	620	73.1	250.2	13.1
15XCJ258A	132.4 o	8	18.8	27.1	3.8	320	630	62.1	240.1	10.1
15XCJ259A	133 o	7	34.3	69	5.3	320	620	61.3	147.4	33.9
15XCJ260A	133.5 o	6	45.4	46.7	12.3	320	620	51	191.5	18.7
15XCJ261A	134 o	8	32.2	39.4	2.7	320	630	58.8	210.2	6.6
15XCJ262A	134.5 o	7	14	37.1	2.9	320	620	70	240.6	9.3
15XCJ263A	135 o	8	38.5	58.2	2.3	320	670	59.7	175.8	24.3
15XCJ264A	135.5 o	8	49.5	46.6	3.3	320	630	47.7	189.2	21.1
15XCJ265A	136 o	7	-4.3	53.7	2.2	320	620	85.8	338.7	27.5
15XCJ269A	138.5 o	8	22.3	34.7	2.7	320	670	63.8	227.9	2.7
15XCJ270A	139.5 o	9	39.6	17.5	3	320	670	44.7	219.6	22
15XCJ271A	140.5 o	7	28.9	62.7	5.8	320	620	66.9	164	27.3
15XCJ272A	141.5 o	8	2.9	24.7	2.2	320	670	66.2	275	22.2
15XCJ273A	142.5 o	9	46	29.6	2.7	320	670	44.4	206.5	18.3
15XCJ274A	143.5 o	7	50.8	62.9	2.9	320	620	51.3	164.3	31.5
15XCJ275A	144.5 o	7	30.6	14.3	1.9	320	620	49.6	230.9	21.7
15XCJ276A	145.5 o	8	5.9	43.2	1.7	320	630	77.5	256.5	16.9
15XCJ278A	147.5 o	8	11.1	28.2	1.5	320	670	66.2	254.6	14.2
15XCJ279A	148.5 o	9	32.8	26.6	0.9	320	670	53.1	221	10.9
15XCJ280A	149.5 o	8	23	42.1	1.2	320	670	66.7	217.4	6.9
15XCJ281A	150.5 o	8	-0.4	30.7	6.6	320	670	69.9	283.1	22.1
15XCJ282A	151.5 o	8	14.1	3.4	1.2	320	630	52.7	258.3	33.7
15XCJ283A	152.5 o	7	49.6	29.8	4.7	320	670	41.7	203.6	21.1

15XCJ284A	153.5 o	8	40.2	22.7	1.8	320	670	46.2	216	18.2
15XCJ285A	154.5 o	8	31.5	39.4	5.4	320	630	59.3	210.8	6.2
15XCJ286A	155.5 o	8	18.3	33.2	1.7	320	670	65.5	236.1	6.3
15XCJ287A	156.5 o	7	29.8	30.9	3.3	320	620	56.9	221.2	5.9
15XCJ288A	157.5 o	8	21.8	45.6	3	320	630	69.2	213.3	10.4
15XCJ289A	158.5 o	8	19.1	35.7	2.9	320	670	66.3	232.2	5.2
15XCJ290A	159.5 o	7	41.9	43.5	1.6	320	620	52.7	197.4	15
15XCJ291A	160.5 o	8	13.6	47.7	1.7	320	630	76.2	222.5	15
15XCJ292A	161.5 o	8	0.6	35	1.3	320	670	72.7	280	20.2
15XCJ293A	162.5 o	7	11.5	40	1.1	320	620	73	243.3	11.9
15XCJ294A	163.5 o	9	23.6	47.9	4.2	320	670	68.8	206.5	12.4
15XCJ295A	164.5 o	8	60	46.2	3.8	320	670	39.2	184	28
15XCJ296A	165.5 o	8	21.8	55.6	2.2	320	670	72.5	187	20.2
15XCJ297A	166.5 o	9	29.2	18.6	1.9	320	670	52.2	230.3	17.2
15XCJ298A	167.5 o	8	55.9	29.1	1.3	320	670	36.4	199.6	26.4
15XCJ299A	168.5 o	7	20.9	45.8	1.6	320	620	70	214	10.9
15XCJ300A	169.5 o	9	223.9	-54.2	5.4	320	520	-54.6	1.6	157.3
15XCJ302A	171.3 o	7	229	-63.8	10.1	320	620	-52.6	342.6	148.3
15XCJ303A	172.5 o	8	171.3	-52.6	1.6	320	630	-82.1	168.9	150.5
15XCJ304A	173.5 o	8	228.9	-16.2	1.8	320	670	-37.4	32.1	151.5
15XCJ306A	175.5 o	8	213.7	-23.5	11.8	320	630	-51.2	42	166
15XCJ307A	176.5 o	7	171	-49.4	7.2	320	620	-80.1	154.2	151.4
15XCJ309A	178.5 o	10	197.5	-26.3	0.6	320	670	-62.4	63	168.5
15XCJ311A	180.5 o	8	199.5	-38.9	7.8	320	670	-67.7	47.5	174.2
15XCJ312A	181.5 o	9	181.5	-20.6	1	320	670	-64	98.7	154.3
15XCJ314A	183.7 o	8	196.6	-40.8	2.9	320	670	-70.5	50.2	171.3
15XCJ315A	184.5 o	8	209	-22.3	3.3	320	630	-53.9	48.3	166.4
15XCJ316A	185.5 o	8	187.9	-36.3	4.4	320	670	-72.2	77	165.8
15XCJ319A	188.5 o	8	27.5	38.1	1.7	320	670	61.7	216.9	3.1
15XCJ320A	189.5 o	8	11.8	56.9	1.9	320	670	80.6	183.3	23.3
15XCJ321A	190.5 o	8	48.9	45.8	2.6	320	630	47.9	190.4	20.5
15XCJ323A	192.5 o	8	194.3	-15.6	8.7	320	630	-58.5	74	157.8
15XCJ326A	195.5 o	7	234.4	-30	2.7	320	620	-37.9	20.1	155.1
15XCJ327A	196.5 o	8	223.1	-34.3	5.3	320	630	-48.4	25.3	165.5
15XCJ328A	197.5 o	8	209.1	-50.9	2.9	320	670	-65.5	15.1	164.3
15XCJ329A	198.5 o	8	245.2	-48.9	5.5	320	670	-36.1	359	148.1
15XCJ331A	200.5 o	8	199	-0.3	6	320	670	-49.5	71.9	144.3
15XCJ332A	201.5 o	7	229.2	-71	4.5	320	620	-52.1	326.3	142.3
15XCJ333A	202.5 o	8	210.2	-52.8	3.3	320	670	-65.2	10.4	162.3
15XCJ334A	203.5 o	8	212.8	-40.7	6.1	320	670	-58.8	28	172.2
15XCJ335A	204.7 o	7	187.8	-52.7	2.6	320	620	-82.8	37.6	158.8
15XCJ336A	205.5 o	8	204.3	-36.6	1.5	320	630	-63.3	42.8	178.6
15XCJ337A	206.4 o	7	208.5	-51.8	1.1	320	620	-66.3	13.8	163.6
16XCJ006A	221 o	7	190.7	-25.2	2.2	320	620	-64.7	76.9	163.7
16XCJ006B	221 o	6	198.6	-37.1	1.5	370	620	-67.3	51.3	174.3
16XCJ008A	224 o	7	179	-3.8	2	320	620	-55.3	103.7	140
16XCJ009A	224.5 o	7	185	-3.9	2.1	320	620	-55	93.2	143.3
16XCJ010A	227.5 o	7	217.1	-35.1	2.4	320	620	-53.3	29.7	170.4
16XCJ011A	228 o	8	219.5	-8.1	2.7	320	620	-41.3	44.3	149.7
16XCJ012A	228.7 o	7	210	-22.3	1.6	320	620	-53.2	47.1	166.2
16XCJ013A	230.1 o	7	204.3	-39.5	1.3	320	620	-64.7	39.3	175.9
16XCJ014A	231 o	6	178.1	-46.2	2.6	370	620	-80.8	112.6	156.9
16XCJ015A	232.1 o	7	240.5	-12.6	1.3	320	620	-27.3	25.2	140.9
16XCJ016A	233.1 o	7	236.5	-27.5	3.9	320	620	-35.3	20.2	152.4
16XCJ016B	233.1 o	6	222.5	-14.2	1.2	370	620	-41.5	38.6	153.7
16XCJ017A	234 o	7	218.1	-47.9	1.6	320	620	-57.3	14.2	164.4
16XCJ018A	235 o	7	220.7	-35.2	2.1	320	620	-50.6	26.5	167.5
16XCJ019A	236.1 o	7	166.5	-24.3	3.9	320	620	-63.2	132.3	144.7
16XCJ020A	237.3 o	6	186.9	-43.9	2.4	320	570	-77.6	71.7	163.5
16XCJ021A	238.5 o	7	201.6	-35.7	1.7	320	620	-64.7	47.9	176.9
16XCJ022A	239.4 o	7	200.7	-15.2	0.7	320	620	-55.5	63.8	159.2
16XCJ023A	239.9 o	7	177.5	-58.7	2.4	320	620	-86.6	247.8	150.5
16XCJ023B	239.9 o	7	205.7	-37.4	3.3	320	620	-62.7	40	178.1
16XCJ024A	241.1 o	6	228.7	-49.1	0.9	370	620	-49.2	6.7	158.2
16XCJ025A	241.7 o	7	239.1	-33.7	2	320	620	-35.5	14.6	152.4
16XCJ026A	242.6 o	7	249.5	-40.7	2	320	620	-29.6	3.7	145.3
16XCJ027A	243.4 o	7	203.6	-26.1	2	320	620	-59	53.2	170.5
16XCJ028A	244.7 o	7	217.5	-50.4	2	320	620	-58.6	10.8	162.7
16XCJ029A	245.5 o	7	190.2	-24.8	2.1	320	620	-64.7	78.3	163
16XCJ031B	247.5 o	7	202.9	-18.6	2.7	320	620	-55.9	58.7	162.9
16XCJ032A	249 o	7	218.4	-32.3	3.6	320	620	-51.2	31	168.8
16XCJ033A	250.5 o	7	213.5	-36.1	1.5	320	620	-56.4	32.4	173.4
16XCJ034A	254 o	7	195.4	-33.8	5.8	320	620	-67.4	61.1	171.6
16XCJ036A	256 o	7	210.9	-41.8	3.8	320	620	-60.7	28.6	172.4
16XCJ037A	257.5 o	7	203.4	-18.3	4.3	320	620	-55.5	58.2	162.7
16XCJ038A	258 o	7	229.2	-16.3	3.2	320	620	-37.2	31.7	151.4
16XCJ040A	260 o	7	28.2	31.7	2.7	320	620	58.4	222.4	4.5
16XCJ041A	262.5 o	7	45.8	27.4	7.9	320	620	43.7	208.2	19.2
16XCJ042A	264 o	7	8	-6.1	2.8	320	620	49.6	269.7	44.7
16XCJ043A	266.25 o	7	39.1	1.9	1.1	320	620	39.2	227.5	36

16XCJ044A	269.2 o	7	38.6	6.5	3.8	320	620	41.3	226	31.4
16XCJ045A	270.1 o	7	30	67.6	1.5	320	620	64.5	149.4	32.2
16XCJ046A	273.3 o	7	-6.8	20.4	5.4	320	620	63.2	296.9	32
45 cutoff										
15XCJ089A	49.5 o	7	215.6	8.7	1.4	320	620	-37.3	55.2	134.8
15XCJ136A	72.5 o	8	74.7	16.8	1.5	320	630	17.3	194.1	47.5
15XCJ140A	74.5 o	8	82.1	24.8	2.6	320	670	14	186	49.5
15XCJ141A	75 o	7	79.4	26.4	4.5	320	620	16.7	186.8	46.6
15XCJ161A	84.5 o	8	140.4	62.1	3.8	320	670	-2.3	129.7	69.4
15XCJ212A	110 o	8	263.3	-23.5	1.7	320	670	-12.6	5.9	128.9
15XCJ240A	123.5 o	9	-17.2	1.5	4.9	320	670	50.8	309.8	52.1
15XCJ241A	124 o	8	-23.3	-11.9	7.1	320	670	42.1	314.1	66
15XCJ310A	179.5 o	8	-69.9	-57.1	4.9	320	670	-8.5	330.6	121.9
15XCJ317A	186.5 o	8	-66	-69.4	2.2	320	670	-16.4	316.8	123.4
15XCJ330A	199.5 o	8	136.3	-55.3	5.2	320	630	-55.1	204.2	130

Sample	Strat. Pos. (	forced? (o=	Number of	Declination	Inclination	MAD	Min Temp i	Max Temp	VGP latitud	VGP Longiti	Angle from the mean
16XXJ004A	13.5	o	7	227.1	-60.9	3	320	650	-53.6	348.4	151.6
16XXJ005A	15.3	o	7	246.8	-18	2.3	320	650	-24.1	18.3	142
16XXJ007A	17	o	7	245.6	-33.8	3.2	320	650	-30.2	10.4	149.6
16XXJ008A	20.4	o	7	236.1	-34.1	4.3	320	650	-37.9	16	157.3
16XXJ009A	21.6	o	7	229.1	-34.9	2.5	320	650	-43.9	20.1	163.2
16XXJ009B	21.6	o	5	16.1	22.1	6.6	320	520	61.1	247.7	17
16XXJ010A	22.4	o	6	34.9	14.8	6	320	650	47	225.6	21.1
16XXJ011A	23.9	o	8	31.3	34.8	3.5	320	650	57.5	215.7	2.3
16XXJ012A	24.9	o	7	45.6	4.1	4.5	320	650	35.6	220.3	34.9
16XXJ013A	26.9	o	7	26.3	42.8	3	320	650	64.7	211.9	7.8
16XXJ014A	28.1	o	7	23.9	43.7	5.1	320	650	66.9	213.4	9.2
16XXJ015A	29.1	o	7	35	6.9	7.2	320	650	43.9	229.2	28.9
16XXJ016A	30	o	7	35	33.8	5.4	320	650	54.4	212.7	5.5
16XXJ017A	31.1	o	7	39.1	60.4	4.2	320	650	59.5	170.6	26.1
16XXJ018A	32.4	o	7	60.4	34.5	4.9	320	650	34.7	193	26.1
16XXJ019A	33.5	o	3	221.8	-14.6	7.2	520	650	-42.1	38.8	156.1
16XXJ021A	38.9	o	7	192	-4.2	4.1	320	650	-53.9	81.2	145.5
16XXJ024A	42	o	7	225.1	-18.1	4.8	320	650	-41	34.1	157.4
16XXJ025B	43	o	7	248.1	-18.8	2.1	320	650	-23.3	17.2	141.4
16XXJ026A	44	o	7	39.7	43.1	4.2	320	650	54.4	199.2	11.7
16XXJ027A	44.9	o	7	64.4	42	5.5	320	650	34.1	185.2	28.7
16XXJ028A	45.8	o	7	47	33.6	2	320	650	45	202.6	15.3
16XXJ029A	46.5	o	5	41.8	51	2.5	320	520	55.3	187.3	18.5
16XXJ030A	47	o	5	26.5	28.3	3.5	320	520	58.1	227.2	7.1
16XXJ031A	48.1	o	4	86.5	52.3	2.5	370	520	21.4	166.1	43.8
16XXJ032A	49.2	o	5	53.8	11.4	2.5	320	520	32.1	210.4	33.1
16XXJ033A	50	o	5	21	36.3	2.4	320	520	65.4	227.8	6.1
16XXJ034A	51.25	o	5	56.1	15.2	2.1	320	520	31.7	206.9	31.7
16XXJ036A	52.9	o	5	59.5	44.4	1.8	320	520	38.9	185.8	25.4
16XXJ037A	54.2	o	5	48.5	33.7	1.7	320	520	43.9	201.5	16.5
16XXJ038A	54.9	o	5	58.1	40.1	2.3	300	450	38.5	190.3	23.8
16XXJ039A	56	o	5	37.9	35.5	5.2	320	520	52.9	208.5	7.6
16XXJ040A	57	o	5	31.2	20.2	2.2	320	520	51.6	226.8	15.2
16XXJ041A	58.5	o	5	34.9	40.2	3.6	320	520	57	206.4	7.1
16XXJ042A	59.1	o	4	51.6	40.1	2.9	320	470	43.7	194.2	18.9
16XXJ043A	59.8	o	4	44.2	37.6	3.5	320	470	48.8	201.4	12.8
16XXJ044A	60.6	o	5	61.1	41.1	3.7	320	520	36.4	187.8	26.2
16XXJ045A	61	o	5	38.3	59.4	3.6	320	520	59.9	173	25
16XXJ046A	61.9	o	5	3.8	29.8	2.8	320	520	69.2	271.5	21.4
16XXJ047A	63.4	o	5	227.9	-21.6	3.8	320	520	-40.1	29.8	158.2
16XXJ048A	63.7	o	5	163.1	-31.2	3.3	320	520	-65.3	143.5	142.2
16XXJ049A	64.2	o	5	265.8	-41.9	2.2	320	520	-17.3	354.2	135.6
16XXJ050A	65.4	o	5	239.9	-7.9	2.8	320	520	-26.3	27.5	140.4
16XXJ051A	66	o	5	246.1	-33.2	3.5	320	520	-29.6	10.5	149
16XXJ052A	67	o	5	248.2	-28	2.3	320	520	-26.2	12.3	145.6
16XXJ053A	67.5	o	5	181.2	-71.6	2.3	320	520	-70.1	283.8	140.9
16XXJ055A	69	o	5	232.1	-13.1	3.3	320	520	-34	30.9	149.3
16XXJ056A	70	o	5	232.9	-8.3	4.2	320	520	-31.8	32.5	145.1
16XXJ057A	71	o	3	227.5	-43.5	3.6	420	520	-48.3	13.5	163.2
16XXJ058A	71.8	o	5	241.1	-24.4	2.6	320	520	-30.7	18.8	149.9
16XXJ059A	73.2	o	5	234.4	-16.7	6.7	320	520	-33.4	27.4	150.4
16XXJ060A	74.2	o	5	233.2	-45.6	2.5	320	520	-44.4	8	158.6
16XXJ061A	75.2	o	5	262.7	-33.8	2.6	320	520	-16.6	0.8	135.9
16XXJ062A	76	o	5	244.5	-37.4	4	320	520	-32.4	8.6	151.1
17XXJ01A	78.5	o	9	231.9	1.9	7.2	300	640	-29.1	37.7	136.9
17XXJ02A	79	o	9	233.4	2.3	4.4	300	640	-27.8	36.6	135.9
17XXJ03A	80	o	9	218.1	-20	1.5	300	640	-46.8	39.5	162.6
17XXJ06A	82.5	o	9	241.9	-11.1	10.1	300	640	-25.8	24.7	141.3
17XXJ07A	83.5	o	9	251.5	-17.7	8.1	300	640	-20.2	15.5	138.1
17XXJ08A	84.5	o	4	224.3	-26.2	6.7	520	640	-44.5	29.9	163.7
17XXJ09A	85.5	o	9	264.1	-37.1	8.7	300	640	-16.7	358.1	135.7
17XXJ10A	86.5	o	10	241.3	-31.6	7.9	300	640	-32.9	14.4	152.5
17XXJ11A	87.1	o	9	243	-54.3	4.4	300	640	-39.7	353.9	149.4
17XXJ12A	88	o	9	246.5	-19	3.6	300	640	-24.7	18	142.8
17XXJ14A	89.75	o	9	227.9	-25	3	300	640	-41.3	27.8	160.5
17XXJ15A	90.5	o	9	221.3	-52.2	5.7	300	640	-56.1	5.7	160.7
17XXJ16A	91	o	9	240.1	-26.3	2.4	300	640	-32.1	18.3	151.5
17XXJ17A	91.75	o	9	261.8	-54	6.5	300	640	-25.6	346.5	138.9
17XXJ18A	92.5	o	9	225	-17.6	4.7	300	640	-40.9	34.4	157.1
17XXJ22A	96	o	9	242.2	-27.2	7.7	300	640	-30.7	16.4	150.2
17XXJ23A	97	o	9	232.9	-63.8	5.2	300	640	-49.8	342	147.8
17XXJ24A	97.5	o	9	246.4	-11.5	3.2	300	640	-22.3	21.6	138.3
17XXJ26A	99.5	o	9	43.1	30.8	5	300	640	47.1	207.8	13
17XXJ27A	100.25	o	9	66.7	21.7	5.8	300	640	25.3	196.6	35.9
17XXJ28A	101	o	8	57.3	26.8	6.6	300	640	34.5	199.9	26
HGX128	108.7	o	4	53.3	14.1	1.8	300	450	33.4	209.5	30.7
HGX125	111.3	o	4	47.5	27.2	0.8	300	450	42.4	206.8	18.1
HGX124	112.2	o	4	55	24.4	3	300	450	35.6	202.9	25.2
HGX122	113.9	o	4	20	5.5	2.3	300	450	51.5	248.5	30.7

HGX121	114.3 o	4	41.8	39.4	1.6	300	450	51.3	201.5	11.4
HGX120	114.9 o	4	55.1	42.9	1.7	300	450	41.9	189.6	21.9
HGX118	116.2 o	4	50.4	11.3	2.9	300	450	34.7	213.1	31.1
HGX116	119.2 o	4	48.1	38	1	300	450	45.8	198.3	15.9
HGX114	120.4 o	4	45.2	30	4.1	300	450	45.1	206.6	15
HGX112	121.7 o	4	58.4	0.4	2.5	300	450	25	211.8	44.5
HGX110	122.9 o	4	75	52.2	3.1	300	450	29.8	171.3	36.8
HGX108	123.9 o	4	32.9	43.3	1.7	300	450	59.7	204.4	8.8
HGX106	125.3 o	4	59	43.1	2.8	300	450	38.8	187.2	24.8
HGX104	126.5 o	4	36.1	47.5	1.7	300	450	58.8	196	13.5
HGX100	131.2 o	4	46.5	-1.7	3.9	300	450	33	222.1	40.6
HGX98	132.7 o	4	2	27.3	3.2	300	450	67.9	276.6	23.9
HGX96	133.5 o	4	25.9	47.6	1.9	300	450	66.9	204.1	12.6
HGX94	134.5 o	4	12.5	43.6	2.5	300	450	74.6	234.3	14.9
HGX91	138.6 o	4	52.4	0	2.1	300	450	29.4	216.5	41.6
HGX87	140.7 o	4	50.1	21.7	2.1	300	450	38.5	208	23.2
HGX85	143.1 o	4	243.4	-6.6	1.8	300	450	-23.2	25.7	137.1
HGX83	145.9 o	4	232.8	-40.3	4.2	300	450	-42.8	13.3	160.2
HGX80	147.7 o	4	246.7	-30.5	3.8	300	450	-28.2	11.8	147.7
HGX78	148.9 o	4	215.8	-2.3	5.8	300	450	-41.6	50.5	146.4
HGX72	152.9 o	4	265.4	-38.7	3.9	300	450	-16.3	356.5	135.1
HGX71	153.2 o	4	241.8	-37.3	3.3	300	450	-34.5	10.3	153.2
HGX65	158 o	4	238.7	-18.4	4.4	300	450	-30.6	23.5	148.4
HGX61	161.7 o	4	256.7	-56.8	4	300	450	-30.5	345.8	141.3
HGX60	162.7 o	4	222.2	-26.7	7.2	300	450	-46.2	31.4	165.5
HGX57	162.9 o	4	236.6	-15.8	5.7	300	450	-31.4	26.2	148.3
HGX52	169.3 o	4	227.4	-27.8	2.8	300	450	-42.7	26.4	162.3
HGX44	171.5 o	4	238.4	-52.6	3.6	300	450	-42.7	357.8	152.6
HGX42	172.2 o	4	240.3	-19.4	4	300	450	-29.7	21.9	147.8
HGX40	172.9 o	4	205.3	-15.3	13.8	300	450	-53.2	56.9	159.9
HGX36	175.3 o	4	46.9	26.4	1.9	300	450	42.6	207.7	18
HGX32	176.9 o	4	62.2	55.5	4.4	300	450	40.7	172.8	30.7
HGX30	177.7 o	4	9.4	40.1	4.8	300	450	74.1	248.7	15.9
HGX28	179.1 o	4	57	19.1	3.8	300	450	32.2	204.3	29.9
HGX24	179.7 o	4	56.1	33.8	1.7	300	450	37.9	196.2	22.7
HGX18	181.9 o	4	48.3	35	5	300	450	44.5	200.6	16.2
HGX16	182.5 o	4	64.2	35.5	2.6	300	450	32	190.1	29
HGX13	185.6 o	4	38.5	37.7	6.5	300	450	53.2	205.9	8.4
HGX10	191.2 o	4	183.2	-46.7	4.7	300	450	-81	83.3	157.8
HGX9	191.5 o	4	236.8	-34.2	2	300	450	-37.5	15.5	156.8
BG1	193.4 o	4	241.2	-16.2	2.9	300	450	-27.9	22.8	145.2
BG2	193.8 o	4	208.2	-21.3	1.1	300	450	-54	49.7	166.1
BG4	194.7 o	4	239.7	-20	9.6	300	450	-30.4	22	148.6
17XXT07A	195 o	4	213.8	-53.2	7.7	480	640	-62.4	7.4	161.6
17XXT06A	197 o	9	254.2	-19.4	5.5	300	640	-18.6	13.1	136.9
BG14	198.7 o	4	200.5	-18.3	0.8	300	450	-57.1	62.3	161.7
17XXT04A	199.5 o	9	234.3	-29.2	8	300	640	-37.7	20.4	157.4
BG18	201.3 o	4	234.5	-13.6	2	300	450	-32.3	28.8	148.1
BG22	204.1 o	4	239	-18.8	1.1	300	450	-30.5	23.1	148.4
17XXT01A	206 o	9	38.4	39.5	7.3	300	640	54	204.2	9
BG26	206.1 o	4	60.8	44.4	0.7	300	450	37.9	185.2	26.2
BG28	207.3 o	4	74.5	53.5	1.4	300	450	30.8	170.1	36.8
BG30	207.9 o	4	22.6	45.7	5.3	300	450	68.7	211.6	11.4
45 cutoff										
16XXJ001A	0.05 o	7	-59.6	21.8	6.9	320	650	31	2.6	76.1
16XXJ003A	13.1 o	7	99.8	-35.4	1.2	320	650	-19.1	202.5	96.9
16XXJ006A	16 o	7	259.4	-17.9	5.3	320	650	-13.9	10.7	131.8
16XXJ022A	40.3 o	7	261.4	-15.3	7.9	320	650	-11.5	10.6	128.9
16XXJ023A	41.1 o	7	256.8	-12.6	5.4	320	650	-14.4	14.6	131
16XXJ025A	42.9 o	7	258.8	-9.6	3.8	320	650	-11.8	14.6	127.6
16XXJ035A	51.9 o	5	79.1	-1.1	2.6	320	520	8.4	198.9	59.5
16XXJ054A	68 o	6	268.2	-49.6	2.3	320	520	-18.9	347.5	134.9
16XXJ065A	10.7 o	5	267.6	0.5	3.2	300	450	-1.8	13.5	114.5
17XXJ04A	81 o	9	265.9	-21.7	6	300	640	-9.9	5.1	128.5
17XXJ05A	82 o	9	266.1	-6.8	6.4	300	640	-5.2	11.5	120.2
17XXJ20A	94 o	3	262.3	-13.5	3.9	560	640	-10.2	10.9	127.1
17XXJ21A	95.25 o	9	119.9	-18.7	4.5	300	640	-29.6	181.4	101.7
17XXJ25A	98 o	9	231.4	4.9	7	300	640	-28.4	39.3	134.5
17XXT03A	201.5 o	9	-76	-42.6	3.6	300	640	-4.1	344	122.7
17XXT05A	199 o	9	-76.9	-14.7	5	300	640	5.9	358	110.9
17XXT08A	192 o	9	-62	-41.2	3.1	300	640	6.1	336.3	112.7
17XXT09A	190 o	9	-30.1	66.6	11.4	300	640	64.9	51.3	45.7
BG6	195.8 o	4	251.8	-10	1.6	300	450	-17.6	18.8	133.3
BG8	196.8 o	4	252.2	3.7	5.4	300	450	-13.1	24.2	123.6
BG10	197.8 o	4	245.9	-4.1	3.6	300	450	-20.5	25.1	133.6
BG12	198.5 o	4	265.9	0	2.8	300	450	-3.3	14.3	116.1
BG16	200.4 o	4	-83.6	-27.8	1.2	300	450	-3.7	356.2	122.7
BG20	203.1 o	4	266.7	-30.9	2.8	300	450	-12.4	0.2	131.7
BG24	205.2 o	4	-34.8	4.5	4.3	300	450	43.1	333.2	65.7
HGX2	194.7 o	4	240	0.3	4	300	450	-23.6	31	133.9

HGX3	194.1 o	4	239.1	28.8	4.6	300	450	-13.9	43.5	109.8
HGX8	191.7 o	4	234.6	22.2	10.2	300	450	-19.7	43.8	117.5
HGX34	175.9 o	4	227	14.1	9.9	300	450	-28	46.6	127.7
HGX38	173.7 o	4	263.8	-0.8	1.6	300	450	-5.3	15.3	118.3
HGX45	170.3 o	4	268	-15	5.2	300	450	-6.1	6.9	123.4
HGX46	169.7 o	4	261.9	-11.1	3.7	300	450	-9.8	12.2	126.1
HGX56	165.1 o	4	263.3	-16.1	4.5	300	450	-10.2	9.2	127.7
HGX62	161.5 o	4	203.6	48.8	4.5	300	450	-20.2	80.2	95.9
HGX66	158.8 o	4	-80.4	7.3	4.5	300	450	9.8	9.1	101
HGX68	156.3 o	4	229.2	39.7	7.8	300	450	-14.9	55.5	102.7
HGX77	149.9 o	4	244.5	25	2.3	300	450	-11.7	38.1	110.8
HGX90	139.2 o	4	150	74.6	2.3	300	450	10.7	116.1	63.7
HGX102	127.7 o	4	79.2	18.2	2.9	300	450	14.2	190.7	47.8